Matter

CellPress

Article

Biomimetic immunomodulation by crosstalk with nanoparticulate regulatory T cells

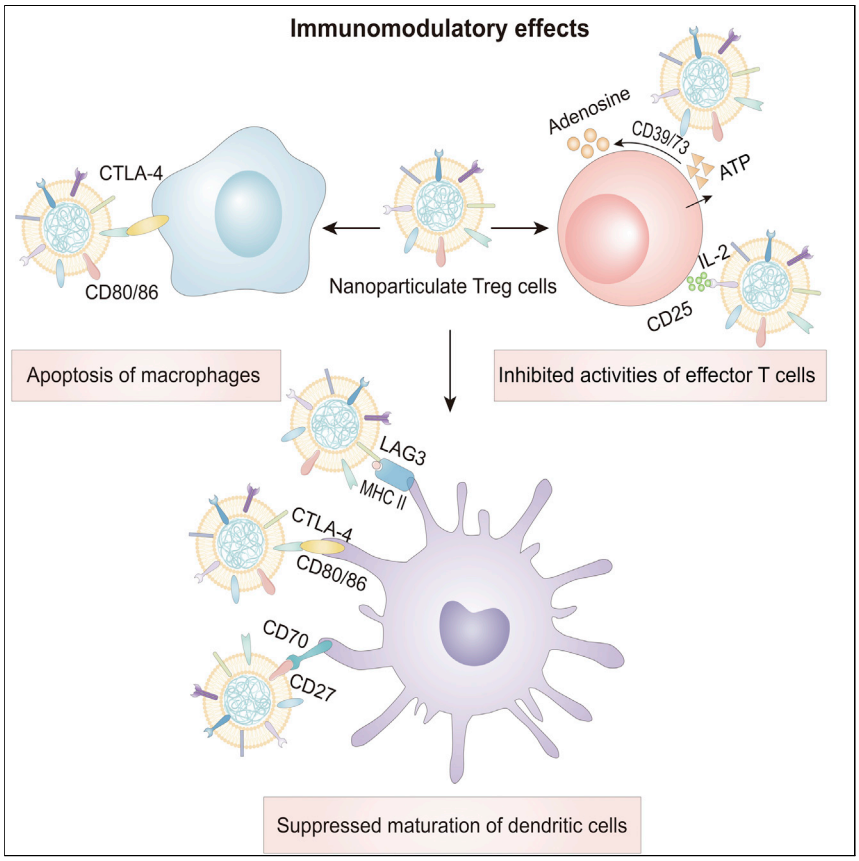

Immuno-inflammatory diseases are critically influenced by overactive immune attacks, but current therapeutic interventions have drawbacks of off-target side effects and inadequate efficacy due to unitary targets. Nanoparticulate regulatory T cells directly crosstalk with multiple immune targets for desirable efficacy in immunosuppression and tissue protection, disclosing a biomimetic immunomodulation strategy for the management of immuno-inflammatory disorders.

Shuang Li, Lu Wang, Yuting Gu, ..., Wei Tao, Eryi Lu, Jinyao Liu

wtao@bwh.harvard.edu (W.T.)
lueryi222@126.com (E.L.)
jyliu@sjtu.edu.cn (J.L.)

Highlights

Direct crosstalk between nanoparticulate regulatory T cells and multiple immune cells

Nanoparticulate cells inhibit the activities of macrophages, dendritic cells, and T cells

Anti-inflammatory and tissue-protective effects achieved in dogs with periodontitis

6 **Development**
Practical, real world, technological considerations and constraints

Li et al., Matter 4, 3621–3645
November 3, 2021
https://doi.org/10.1016/j.matt.2021.08.015

Matter

CellPress

Article

Biomimetic immunomodulation by crosstalk with nanoparticulate regulatory T cells

Shuang Li,[1,2] Lu Wang,[2] Yuting Gu,[1] Lu Lin,[1] Mengmeng Zhang,[2] Min Jin,[1] Chuanyuan Mao,[1] Jun Zhou,[3] Weiqi Zhang,[1] Xiangang Huang,[3] Claudia Corbo,[4] Wei Tao,[3,*] Eryi Lu,[1,*] and Jinyao Liu[2,5,*]

SUMMARY

Hyperactive immunity mediates the development and progression of various immuno-inflammatory diseases. However, the use of immunosuppressive or anti-inflammatory agents has been largely restricted either by off-target side effects or by individual interaction site. Here, we describe a biomimetic manipulation strategy for immunosuppression by crosstalk with regulatory T (Treg) cell membrane-coated nanoparticles. Due to the reservation of intrinsic membrane proteins and function from Treg cells, coated nanoparticles can directly interact with multifaceted overactive immune cells. By virtue of this unique characteristic, nanoparticulate Treg cells inhibit macrophage-osteoclast differentiation, the maturation of dendritic cells, and the activation of effector T cells. In both murine and canine models of periodontitis, these nanoparticles successfully suppress excessive immune responses, alleviating inflammation and curbing alveolar bone resorption. Our work reveals how dysregulated immune responses can be effectively manipulated by biomimetic immunomodulation and proposes the utilization of nanoparticulate Treg cells as a promising approach to treat immuno-inflammatory diseases.

Progress and potential

A biomimetic strategy for modulating various dysregulated immune responses is demonstrated by crosstalk with regulatory T cell membrane-coated nanoparticles. Biomimetic immunomodulation suggests its ability to alleviate immuno-inflammatory responses and protect inflamed tissue in a large animal model of chronic periodontitis. Nanoparticulate regulatory T cells show clinical translational potential for the management of immuno-inflammatory disorders.

INTRODUCTION

The immune system plays a central role in maintaining tissue homeostasis and mediating a wide range of disease processes. Autoimmune syndromes and chronic inflammatory diseases typically suffer from hyperactive immune responses at various tissue sites.[1–4] The intricate immune responses dictated by overactive innate and adaptive immune cells tend to elicit a cascade of inflammatory activities to cause tissue damage and disease progression.[5–7] As for current interventions, upstream approaches, such as systemic administration of wide-spectrum immunosuppressive drugs, are inevitably limited by rapid clearance as well as systemic side effects, including opportunistic infections and malignancy.[8] Conversely, downstream methods such as anti-inflammatory agents interact solely with individual targets in the complex and heterogeneous inflammatory network, eliciting only weak inhibitory effects.[9,10] Therefore, alternative strategies that overcome these limitations are necessary to improve the management of hyperactive immunity-related disorders.

Recent advances in the fields of nanotechnology and bioengineering afford attractive opportunities to improve the safety and effectiveness of immunoregulation and anti-inflammation by precision interventions.[11] The development of nanoplatforms to deliver immunosuppressants or anti-inflammatory agents can considerably

reduce their off-target effects and systemic toxicity.[12] Nanoparticle (NP)-assisted immunomodulation has been explored to produce immune tolerance by modulating the anti-inflammatory polarization of macrophages, inducing the expansion of regulatory T (Treg) cells, or generating tolerogenic dendritic cells.[13–16] Unfortunately, NP-based delivery often requires frequent and long-term high dosing but is still insufficient to bypass the innate shortcomings of immunosuppressive or anti-inflammatory agents.[17–19] On the other hand, emerging anti-inflammatory approaches have been designed to exploit decorated NPs as decoys to neutralize proinflammatory cytokines by specific ligand-receptor interactions.[20,21] Despite the appeal of decreasing the exposure of proinflammatory cytokines, immunomodulatory NPs are not competent to interact directly with the upstream hyperresponsive immune cells responsible for the production of various cytokines.[22] Furthermore, such bioengineered NPs are intended for targeting a single immune cell type, and the elicited tolerogenic phenotypes are subject to instability, given microenvironments abounding with proinflammatory cytokines.[23–25] Thus, methods for modifying multiple dysregulated immune cell behaviors are of great importance for efficaciously suppressing excess immune activation.

Maintenance of immune homeostasis relies on orchestrated immune responses.[26] Treg cells, a dominant immunosuppressive T cell subset, provide immunological balance by suppressing effector immune cells or by eliminating aberrant self-attacking clones.[27] In addition to exploiting the mechanism of suppressive cytokine production, Treg cells notably confer immune tolerance in a contact-dependent manner against various activated immune cells by virtue of functional ligands on their cell surface. Inspired by the crosstalk between Treg cells and other immune cells, we speculate that Treg cell membrane-coated NPs (TNPs) could be developed as a biomimetic immune-engineering strategy to suppress broad-spectrum excessive immune responses, which may be useful in treating immuno-inflammatory diseases. Here, we report the use of nanoparticulate Treg cells to crosstalk with multiple provoked immune cells, which mimics the immunoregulation normally mediated by Treg cells. TNPs decorated with surface proteins and membrane function from Treg cells exert multifaceted suppressive effects on target immune cells to dampen overactive immune responses (Figure 1A). First, TNPs potently inhibit macrophage-osteoclast differentiation via direct contact with costimulatory molecules, activating downstream events that induce the apoptosis of macrophages. Furthermore, TNPs bind to costimulatory signals on the surface of dendritic cells (DCs) to suppress their maturation. In addition, TNPs exhibit regulatory effects on the proliferation and cytokine secretion of effector T cells. *In vivo* administration of TNPs in murine models of both early and advanced stages of periodontitis consistently validates the beneficial effects of TNPs on mitigating immuno-inflammatory responses and reducing alveolar bone resorption. Remarkably, TNPs also display anti-inflammatory and tissue-protective effects in a preclinical canine model of periodontitis. The current study highlights the impact of biomimetic immunoregulation and the therapeutic potential of TNPs in immuno-inflammatory diseases.

RESULTS AND DISCUSSION

Preparation and characterization of TNPs

Cell membrane coating has recently emerged as a promising platform to leverage functional antigens on natural cell membranes to endow NPs with specific bioactivities.[28] To prepare TNPs, cluster of differentiation 4 (CD4), CD25, and forkhead box P3 (Foxp3)-positive ($CD4^+CD25^+Foxp3^+$) Treg cells were purified from mouse splenocytes and expanded *in vitro* (Table S1; Figures 1A and S1A), after which Treg cell

[1]Department of Stomatology, Renji Hospital, School of Medicine, Shanghai Jiao Tong University, Shanghai 200127, China

[2]Shanghai Key Laboratory for Nucleic Acid Chemistry and Nanomedicine, Institute of Molecular Medicine, State Key Laboratory of Oncogenes and Related Genes, Shanghai Cancer Institute, Renji Hospital, School of Medicine, Shanghai Jiao Tong University, Shanghai 200127, China

[3]Center for Nanomedicine and Department of Anesthesiology, Brigham and Women's Hospital, Harvard Medical School, Boston, MA 02115, USA

[4]School of Medicine and Surgery, Nanomedicine Center Nanomib, University of Milano-Bicocca, Vedano al Lambro 20854, Italy

[5]Lead contact

*Correspondence: wtao@bwh.harvard.edu (W.T.), lueryi222@126.com (E.L.), jyliu@sjtu.edu.cn (J.L.)

https://doi.org/10.1016/j.matt.2021.08.015

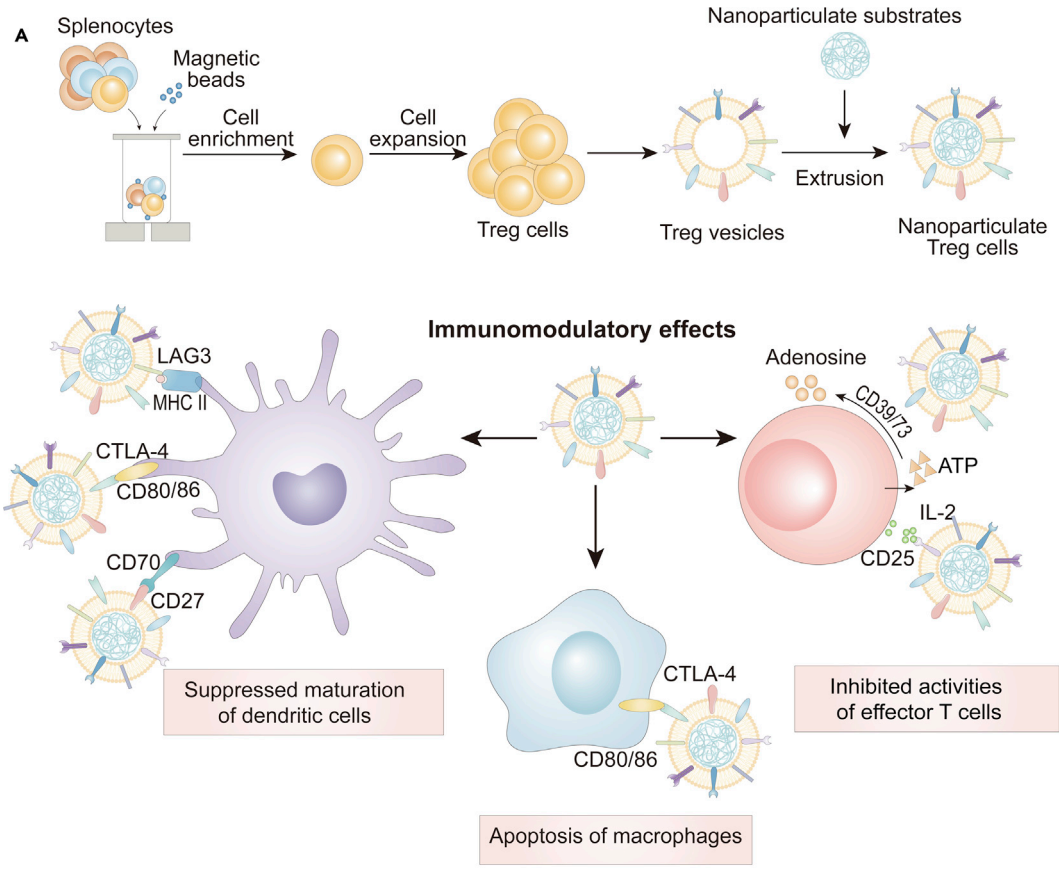
A
Splenocytes
Magnetic beads
Cell enrichment
Cell expansion
Treg cells
Nanoparticulate substrates
Extrusion
Treg vesicles
Nanoparticulate Treg cells
Immunomodulatory effects
LAG3
MHC II
CTLA-4
CD80/86
CD70
CD27
Suppressed maturation of dendritic cells
Adenosine
CD39/73
ATP
IL-2
CD25
Inhibited activities of effector T cells
CTLA-4
CD80/86
Apoptosis of macrophages

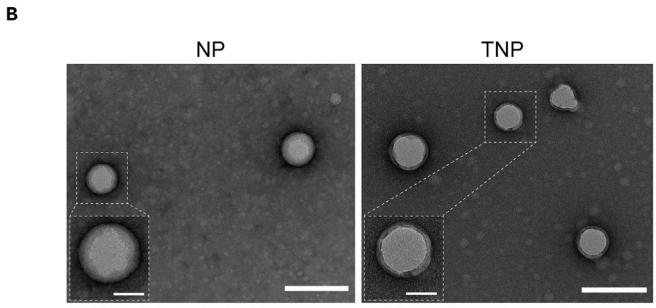
B
NP
TNP

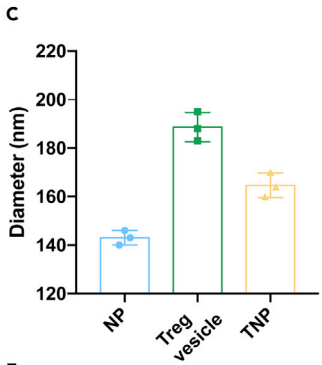
C
Diameter (nm)
220
200
180
160
140
120
NP
Treg vesicle
TNP

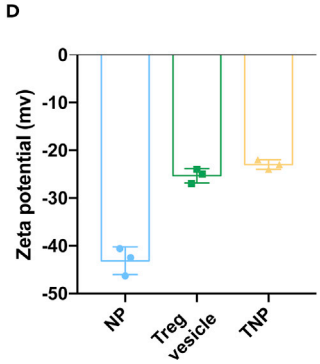
D
Zeta potential (mv)
0
-10
-20
-30
-40
-50
NP
Treg vesicle
TNP

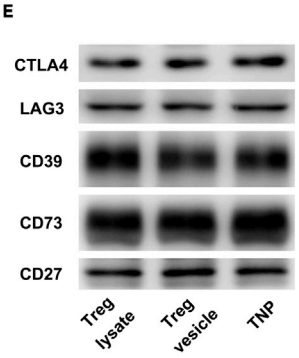
E
CTLA4
LAG3
CD39
CD73
CD27
Treg lysate
Treg vesicle
TNP

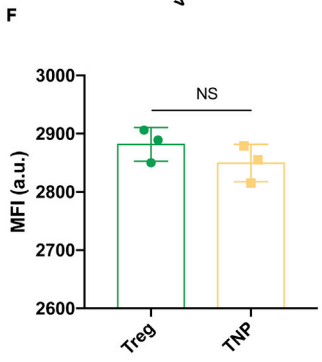
F
MFI (a.u.)
3000
2900
2800
2700
2600
NS
Treg
TNP

Figure 1. Preparation and characterization of TNPs

(A) Schematic illustration of nanoparticulate Treg cells designed for suppressing multiple excessive immune responses.

(B) Representative TEM images of NPs and TNPs stained with uranyl acetate. Scale bar: 200 nm. Inset: zoomed-in view of a single NP and TNP. Scale bar: 50 nm.

(C and D) Results of (C) hydrodynamic size and (D) zeta potential of TNPs measured by DLS.

(E) Characteristic membrane protein markers of Treg lysates, Treg membrane vesicles, and TNPs detected by western blot assay.

(F) MFIs of Treg cells (1.5×10^6 cells suspended in 100 μL of PBS) and TNPs (100 μL of suspension with a protein concentration of 0.1 mg/mL) stained with PE-labeled anti-mouse CTLA-4 antibody. Data are shown as mean ± SD. Statistical significance was analyzed by the two-tailed t test. NS, no significance.

membranes were harvested and coated onto poly(lactic-co-glycolic acid) (PLGA) nanoparticulate cores via extrusion (Figure 1A; Table S2). Transmission electron microscopy (TEM) images of the synthesized TNPs after uranyl acetate staining demonstrated that Treg membranes were fully wrapped around the PLGA cores (Figure 1B), presenting a typical core-shell morphology[29] distinct from the bare core structure of PLGA NPs. The structure of TNPs was further imaged by cryogenic TEM (cryo-TEM) (Figure S2), showing a coating of unilamellar lipid layer with a thickness of 6–8 nm, similar to that of cell membranes.[30] Dynamic light scattering (DLS) results in Figure 1C revealed that the hydrodynamic size of NPs was increased after coating. NP tracking analysis (NTA) further disclosed the size increment of TNPs compared with NPs (Figure S3) and that there was ~8% of Treg vesicles within the TNP mixture. The surface zeta potential of TNPs was less negative than that of NPs and resembled that of Treg membrane-derived vesicles (Figure 1D). Moreover, TNPs exhibited desirable colloidal stability with limited fluctuation in both size and size distribution over a period of 28 days (Figure S4). In addition, western blot results corroborated the presence of characteristic membrane proteins derived from Treg cell membranes, including cytotoxic T lymphocyte-associated protein (CTLA-4), lymphocyte-activation gene 3 (LAG3), CD39, CD73, and CD27, further indicating the successful coating of Treg membranes onto NPs (Figures 1E, S5, and S6). Moreover, the outward orientation of the surface proteins on TNPs was confirmed by immunostaining of CTLA-4 on TNPs and Treg cells with an equivalent amount of membrane proteins. Quantitative median fluorescence intensity (MFI) results from flow cytometric analysis showed no significant difference between these two groups (Figure 1F). Cell membrane glycoproteins on TNPs were verified to be right side out as indicated by similar wheat germ agglutinin (WGA) fluorescence intensity to Treg cells with equivalent membrane proteins (Figure S7). These results demonstrated that the membrane proteins on TNPs were oriented outward, similarly to those on Treg cells, due to the electrostatic effects between NP cores and the cell membranes with abundant sialylated moieties on the surface.[31] Proper orientation on TNPs would guarantee the exertion of the biological functions of the membrane protein ligands.[32,33] In addition, TNPs presented satisfying storage stability at −80°C with negligible loss of protein content and variation on functions within 4 weeks (Figure S8). Importantly, TNPs exhibited no apparent cytotoxicity *in vitro* (Figure S9).

TNPs inhibit osteoclast differentiation of macrophages

A critical link has been documented between the adaptive immune system and bone resorption.[34,35] To verify the interplay between TNPs and macrophages, fluorescently labeled TNPs and NPs were incubated with macrophages and subjected to confocal observation. As shown in Figure 2A, many more TNPs adhered to the cell membranes of macrophages compared with NPs. Flow cytometric analysis further verified that macrophages treated with TNPs exhibited significantly more MFI than their NP counterparts (Figure 2B). These results suggested the capacity of TNPs to specifically bind to macrophages. Furthermore, macrophages were induced

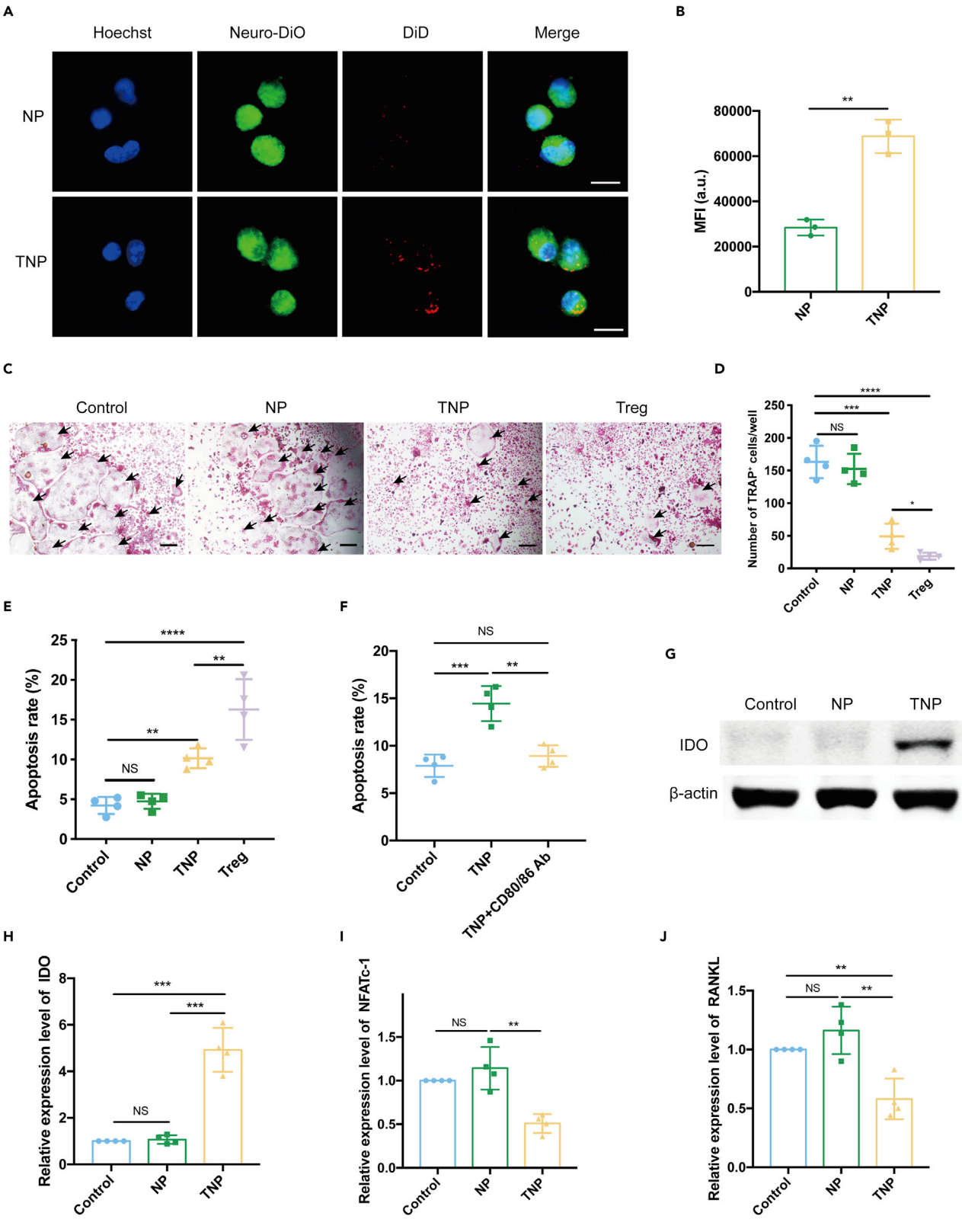
A
Hoechst
Neuro-DiO
DiD
Merge
NP
TNP
B
MFI (a.u.)
80000
60000
40000
20000
0
**
NP
TNP
C
Control
NP
TNP
Treg
D
Number of TRAP+ cells/well
250
200
150
100
50
0
****
***
NS
*
Control
NP
TNP
Treg
E
Apoptosis rate (%)
25
20
15
10
5
0
****
**
**
NS
Control
NP
TNP
Treg
F
Apoptosis rate (%)
20
15
10
5
0
NS
***
**
Control
TNP
TNP+CD80/86 Ab
G
Control
NP
TNP
IDO
β-actin
H
Relative expression level of IDO
8
6
4
2
0
***
***
NS
Control
NP
TNP
I
Relative expression level of NFATc-1
1.5
1.0
0.5
0.0
NS
**
Control
NP
TNP
J
Relative expression level of RANKL
1.5
1.0
0.5
0.0
**
NS
**
Control
NP
TNP

Figure 2. TNPs inhibit macrophage-osteoclast differentiation

(A) Typical confocal images of macrophages after incubation with TNPs or NPs. Blue, green, and red represents cell nuclei, cell membranes, and NPs, respectively. Scale bar: 10 μm.

(B) Quantification of NPs bound to macrophages by flow cytometric analysis (n = 3, unpaired two-tailed t test).

(C) Representative TRAP staining images for osteoclasts after treatments with NPs, TNPs, and Treg cells with equivalent membrane proteins. Scale bar: 200 μm.

(D and E) (D) Quantification of $TRAP^+$ multinucleated osteoclast cells after various treatments (n = 4, one-way ANOVA with Tukey test). (E) Quantification of apoptosis rate of macrophages after incubations with NPs, TNPs, and Treg cells with equivalent membrane proteins for 24 h by flow cytometric analysis (n = 4, one-way ANOVA with Tukey test).

(F) Apoptosis rate of macrophages after incubation with TNPs in the absence or presence of CD80/86 blocking antibodies for 24 h by flow cytometric analysis (n = 4, one-way ANOVA with Tukey test).

(G) Representative western blot images of IDO and β-actin protein expression in macrophages incubated with TNPs or NPs for 3 days.

(H–J) Relative mRNA expression levels of (H) IDO, (I) NFATc-1, and (J) RANKL in macrophages treated with TNPs or NPs for 3 days by qPCR analysis (n = 4, one-way ANOVA with Tukey test).

All data are represented as means ± SD. *p < 0.05, **p < 0.01, ***p < 0.001, ****p < 0.0001. NS, no significance.

for osteoclast differentiation in the presence of TNPs or NPs. After induction for 5 days, osteoclast formation was assessed by tartrate-resistant acid phosphatase (TRAP) staining. TRAP staining images (Figure 2C) and quantitative analysis (Figure 2D) indicated that both TNPs and Treg cells robustly reduced the number of $TRAP^+$ multinucleated osteoclasts induced by macrophage colony stimulating factor (MCSF) and receptor activator of nuclear factor kappa-B ligand (RANKL), compared with phosphate-buffered saline (PBS) control and NP groups.

Next, we examined the effects of TNPs and Treg cells on the apoptosis of macrophages via flow cytometric analysis. Significantly increased staining intensity of annexin V (Figure S10A) together with quantitative results (Figure 2E) reflected that TNP- and Treg-cell-treated macrophages suffered a higher apoptosis rate than those treated with NPs or PBS, indicating that TNPs inherited the membrane proteins from source Treg cells to induce the apoptosis of macrophages. It was postulated that TNPs could target CD80/86 on osteoclast precursors to inhibit osteoclastogenesis.[36] To test this hypothesis, macrophages were pretreated with neutralization antibodies CD80 and CD86 for binding site blockade and incubated with TNPs for 24 h. Flow cytometry demonstrated that the distinctly increased apoptosis of macrophages resulting from TNP incubation was abrogated by CD80/86 blockade (Figures 2F and S10B), implying that TNPs specifically targeted CD80/86 on macrophages to suppress osteoclastogenesis. To elucidate the downstream molecular mechanism, the gene and protein expression in macrophages treated with TNPs or NPs were investigated by real-time quantitative polymerase chain reaction (qPCR) and western blot, respectively. The protein expression (Figure 2G) and relative mRNA expression level (Figure 2H) of indoleamine 2,3-dioxygenase (IDO) were both substantially upregulated. In addition, the IDO expression kinetics in macrophages after TNP treatment was further examined. Compared with the control group (0 h), TNP treatment for 24, 48, and 72 h stimulated a constant upregulation of IDO expression in macrophages (Figure S11). Such elevated tryptophan catabolism could be caused by the engagement of CD80/86 on macrophages and CTLA-4 on TNPs, and thus lead to macrophage apoptosis as well as impaired osteoclast differentiation.[37,38] In addition, the downregulation of osteoclast-related genes, including nuclear factor of activated T cells 1 (NFATc-1) (Figure 2I) and RANKL (Figure 2J), in macrophages treated with TNPs further supports the inhibitory effect of TNPs on osteoclast differentiation. Collectively, these results suggested that TNPs specifically targeting the costimulatory molecules CD80/86 on macrophages potently suppressed osteoclastogenesis via upregulated expression of IDO to further induce macrophage apoptosis, offering an alternative strategy to modulate osteoclast differentiation of macrophages from the osteoimmunology perspective.

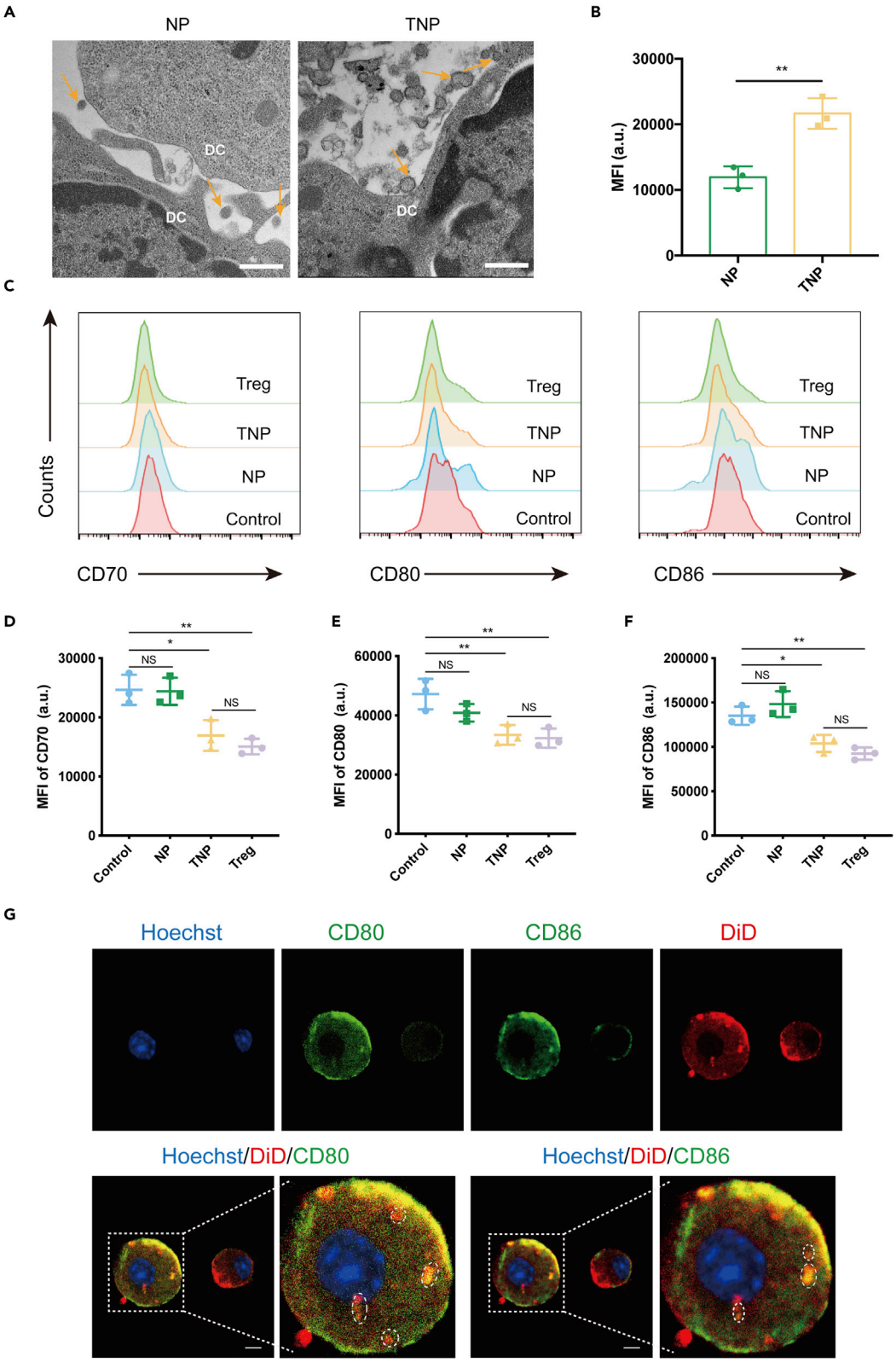
A
NP
TNP
DC
DC
DC
B
MFI (a.u.)
30000
20000
10000
0
**
NP
TNP
C
Counts
Treg
TNP
NP
Control
CD70
CD80
CD86
D
MFI of CD70 (a.u.)
30000
20000
10000
0
**
*
NS
NS
Control
NP
TNP
Treg
E
MFI of CD80 (a.u.)
60000
40000
20000
0
**
**
NS
NS
F
MFI of CD86 (a.u.)
200000
150000
100000
50000
0
**
*
NS
NS
G
Hoechst
CD80
CD86
DiD
Hoechst/DiD/CD80
Hoechst/DiD/CD86

Figure 3. TNPs suppress the maturation of DCs

(A) Representative TEM images of DCs after incubation with TNPs or NPs at 4°C for 1 h. Orange arrowheads indicate the NPs around DCs. Scale bar: 500 nm.

(B) Flow cytometric analysis of the binding of TNPs or NPs to DCs (n = 3, unpaired two-tailed t test).

(C) Flow cytometric profiles of CD70, CD80, and CD86 on DCs after incubation with NPs, TNPs, and Treg cells with equivalent membrane proteins for 48 h.

(D–F) MFI quantification of (D) CD70, (E) CD80, and (F) CD86 on DCs after cultures with NPs, TNPs, and Treg cells with equivalent membrane proteins (n = 3, one-way ANOVA with Tukey test).

(G) Immunofluorescence images of CD80 and CD86 on DCs and TNPs after coincubation at 4°C for 1 h observed via confocal imaging (top). Yellow indicates the colocalization of TNPs (red) with CD80 or CD86 (both green). Typical colocalization patches were marked with white dashed circles in the enlargement of the boxed area (bottom). Scale bar: 5 μm. All data are represented as means ± SD. *$p < 0.05$, **$p < 0.01$. NS, no significance.

TNPs suppress the maturation of DCs

It is well established that Treg cells exert suppressive effects on antigen-presenting cells (APCs) in a cell-contact-dependent manner through the interaction between cell membrane proteins.[39] Therefore, TNPs might also influence the behavior of APCs, particularly DCs, through the interaction between cell membrane proteins from both sides. To determine whether TNPs directly bind to DCs, cells incubated with coated NPs or bare NPs for 1 h were imaged by TEM. The results indicated that more TNPs were bound to the surface of DCs than to NPs (Figure 3A). Moreover, DCs were incubated with fluorescently labeled NPs to quantify binding by flow cytometry. Compared with NPs, the higher MFI of DCs ($p < 0.01$) indicated that TNPs specifically targeted the cell membrane of DCs (Figure 3B). To determine the effect of close contact, we attempted to examine the expression of costimulatory molecules, including CD70, CD80, and CD86, on the membrane of DCs after incubation with TNPs or NPs. Flow cytometric histogram (Figure 3C) and quantitative MFI analysis (Figures 3D–3F) revealed that, similar to the immunosuppressive capacity of Treg cells on the costimulatory signals on DCs, TNPs significantly downregulated the expressions of CD70 (Figure 3D), CD80 (Figure 3E), and CD86 (Figure 3F) on DCs compared with NP and control groups. In addition, there was no apparent difference between TNPs and Treg cells with equal membrane proteins in inhibiting costimulatory signals. To explore the underlying mechanism and the downregulation of surface costimulatory molecules, immunofluorescence staining of CD80 and CD86 on DCs was conducted after incubation with fluorescently labeled TNPs at 4°C for 1 h. As displayed in Figure 3G, the close interaction between TNPs (red) and CD80 or CD86 (both green) could be interpreted by the colocalization (yellow) of fluorescence signals. The colocalization between TNPs and CD80 or CD86 was further quantitatively analyzed using the metric of Manders' colocalization coefficient (MCC). As demonstrated in Figure S12, the MCC values for TNPs/CD80 and TNPs/CD86 were both close to 1, indicating a high colocalization and close contact between TNPs and CD80/CD86.[40] Furthermore, we examined the gene expression of these costimulatory molecules in DCs after treatment with TNPs for 48 h by qPCR. Results shown in Figure S13 demonstrated that only the mRNA level of CD80 exhibited an overt increase compared with the other two groups, and there was a negligible difference in the transcriptional levels of CD70 and CD86 among all groups. Taken together, with the help of surface proteins conferred by Treg cell membranes, TNPs inhibited the maturation of DCs by directly binding with their membrane costimulatory molecules. We speculated that CTLA-4 on TNPs could capture the ligands such as CD80 and CD86 on DCs by a process of trans-endocytosis, while surface CD27 could also induce the internalization of CD70 into DCs,[41,42] thus reducing the membrane protein level of these costimulatory molecules and further inhibiting the maturation of DCs. Meanwhile, LAG3 on TNPs could directly act on the major

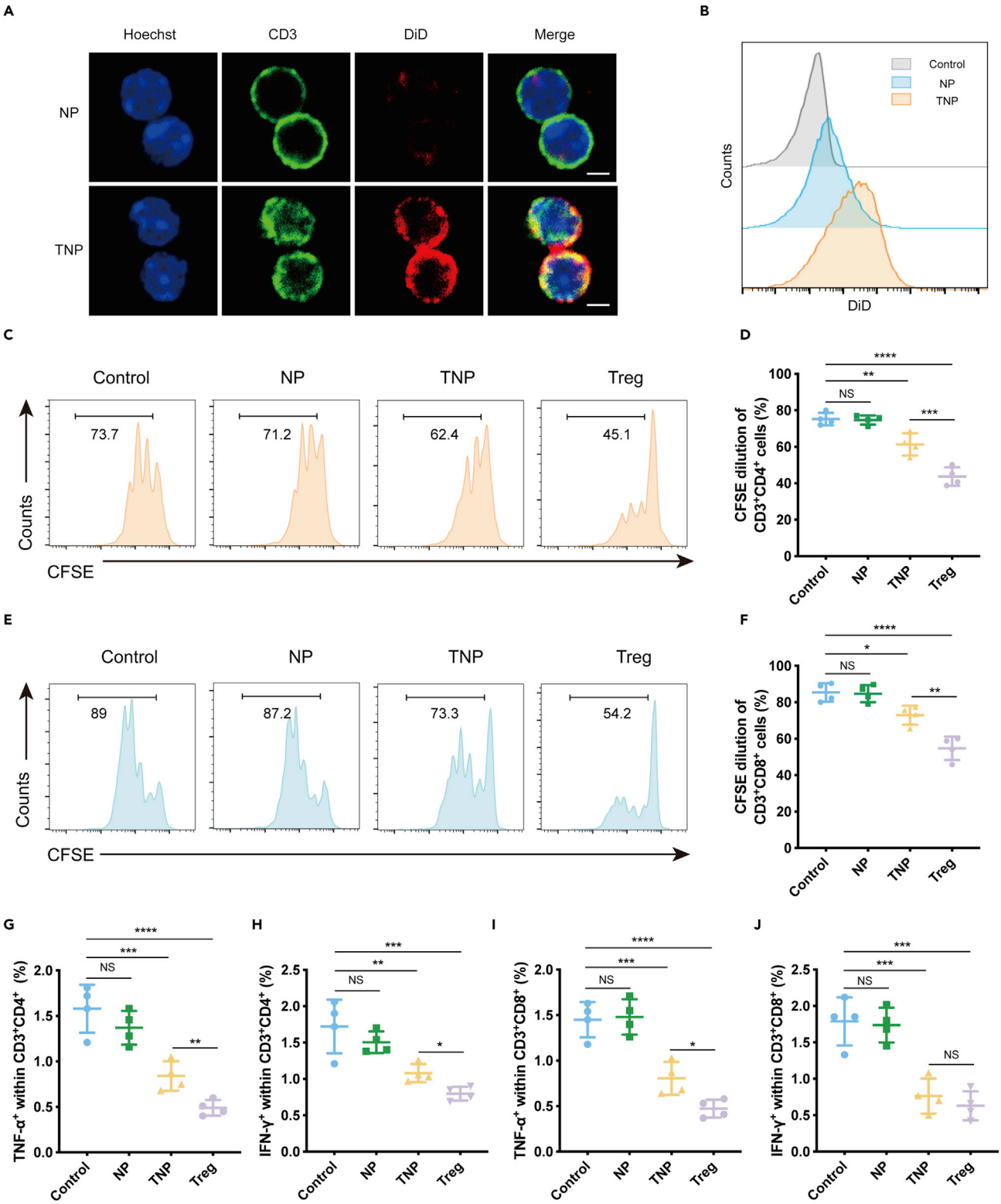

Figure 4. TNPs suppress the proliferation and activation of T cells

(A) Typical confocal images of $CD3^+$ T cells incubated with TNPs or NPs. Blue, green, and red represent cell nuclei, FITC-conjugated anti-CD3 antibody, and the NPs, respectively. Scale bar: 2 μm.

Figure 4. *Continued*

(B) Representative flow cytometric plots of T cells bound with TNPs or NPs after coincubation at 4°C for 1 h.

(C–F) Representative flow cytometric plots and quantitative analysis of the CFSE dilution of (C, D) the labeled $CD4^+$ and (E, F) $CD8^+$ T cells after incubation with NPs, TNPs, and Treg cells with equivalent membrane proteins in the presence of CD3, CD28, and IL-2 for 96 h.

(G–J) Fractions of (G) $CD4^+TNF\text{-}\alpha^+$ and (H) $CD4^+IFN\text{-}\gamma^+$ T cells of total $CD4^+$ T cells and percentages of (I) $CD8^+TNF\text{-}\alpha^+$ and (J) $CD8^+IFN\text{-}\gamma^+$ T cells of total $CD8^+$ T cells following cultivation with NPs, TNPs, and Treg cells with equivalent membrane proteins in the presence of CD3, CD28, and IL-2 for 96 h, as assessed by flow cytometric analysis. Error bars represent ±SD. n = 4. Significance was assessed using one-way ANOVA with Tukey test. *$p < 0.05$, **$p < 0.01$, ***$p < 0.001$, ****$p < 0.0001$. NS, no significance.

histocompatibility complex class II (MHC II) to trigger the inhibitory pathway, suppressing the maturation and immunostimulatory function of DCs.[43]

TNPs inhibit the proliferation and activation of T cells

To investigate whether TNPs could directly affect T cells, splenocytes isolated from naive mice were incubated with fluorescently labeled TNPs or NPs for confocal imaging. Different from the limited nonspecific adherence of NPs to $CD3^+$ T cells, there were many TNPs tightly bound to the membrane of T cells (Figure 4A), suggesting specific interplay. The cells were also cultivated with the labeled TNPs or NPs to quantify the binding of NPs with $CD3^+$ T cells. Flow cytometric analysis confirmed that T cells treated with TNPs presented significantly higher MFI relative to NPs ($p < 0.001$), further confirming their close communication (Figures 4B and S14). We then assessed the immunosuppressive effects of TNPs toward effector T cells activated with CD3 and CD28. The proliferation activity of T cells after TNP treatment was analyzed by carboxyfluorescein succinimidyl ester (CFSE) assay. As shown in Figures 4C–4F, both TNPs and Treg cells caused significantly lowered dilution ratios of CFSE-labeled $CD3^+CD4^+$ T subset (Figures 4C and 4D) and $CD3^+CD8^+$ T population (Figures 4E and 4F) in contrast to the control and NP groups. Flow cytometric analysis further showed that, similar to Treg cells, TNPs markedly restricted the fractions of $Ki67^+$ (Figures S15A and S15B) as well as tumor necrosis factor alpha-positive ($TNF\text{-}\alpha^+$) and interferon-gamma-positive ($IFN\text{-}\gamma^+$) cells among all $CD3^+CD4^+$ cells compared with those treated with NPs and PBS (Figures 4G, 4H, S16A, and S16B), implying that TNPs could reduce the proliferation and cytokine production of $CD4^+$ T cells. Similar results were obtained for the proliferative and activating responses of the $CD3^+CD8^+$ compartment (Figures 4I, 4J, S15C, S15D, S16C, and S16D). It is worth noting that CD39 and CD73 are extracellular nucleotide-catabolizing enzymes that endow Treg cells with suppressive function by sequentially degrading extracellular adenosine triphosphate (ATP) leaking from activated cells.[44,45] Therefore, it was assumed that TNPs carrying CD39 and CD73 tended to closely aggregate on effector T cells to hydrolyze ATP released to pericellular sites, thereby potentially inhibiting the proliferation and inflammatory cytokine secretion of T cells.

Immunoregulation mediated by TNPs in two murine models of periodontitis

The efficacy of TNPs to inhibit various immune responses to alleviate inflammation and periodontal tissue damage was evaluated in mouse models of advanced and early periodontitis induced by ligature placement for 30 days and 10 days, respectively. The local retention and biodistribution of DiR-labeled TNPs were analyzed by *in vivo* imaging system (IVIS), revealing that over 60% of TNPs remained in local sites 48 h post injection, while part of the NPs distributed in the draining cervical lymph nodes (CLNs) and major organs, including liver, lung, and spleen (Figure S17).

After the induction of advanced periodontitis, TNPs were injected into the inflamed periodontal tissue at indicated time points to analyze the possible alleviation of periodontal inflammation and tissue protection (Figures 5A and 5B). Mice treated with

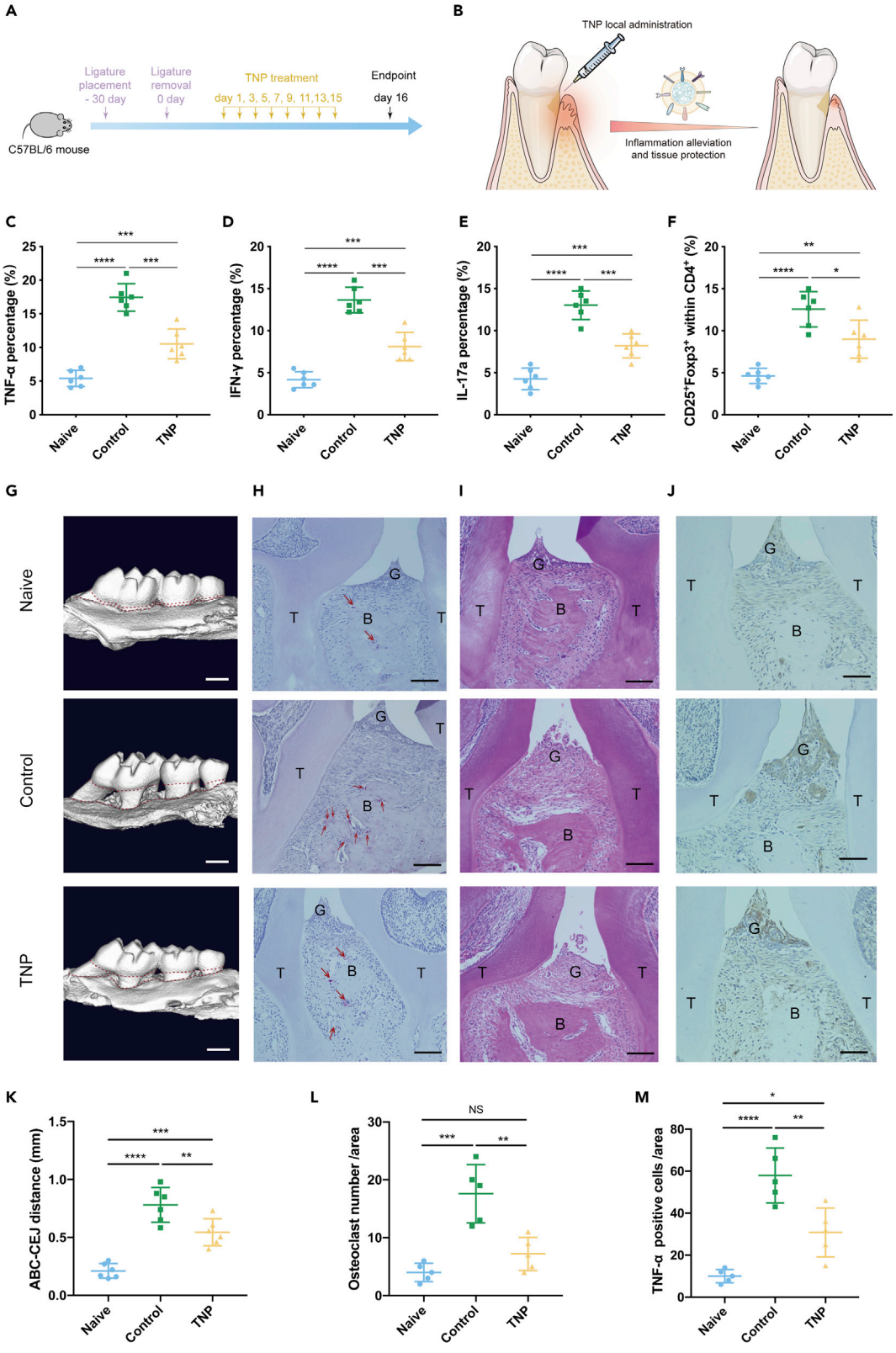
A
Ligature placement - 30 day
Ligature removal 0 day
TNP treatment
day 1, 3, 5, 7, 9, 11,13,15
Endpoint
day 16
C57BL/6 mouse
B
TNP local administration
Inflammation alleviation and tissue protection
C
TNF-α percentage (%)
D
IFN-γ percentage (%)
E
IL-17a percentage (%)
F
CD25+Foxp3+ within CD4+ (%)
Naive
Control
TNP
G
H
I
J
K
ABC-CEJ distance (mm)
L
Osteoclast number /area
NS
M
TNF-α positive cells /area

Figure 5. TNPs alleviate immuno-inflammatory responses and reduce alveolar bone resorption in a mouse model of advanced periodontitis

(A) Experimental design of the treatment regimen of TNPs for a mouse model of advanced periodontitis induced by the placement of ligature around the maxillary first molar for 30 days. Mice dosed with PBS were used as a control.

(B) Schematic illustration of effects of local TNP administration on periodontal inflammation alleviation and tissue protection.

(C–F) Percentages of (C) $CD4^+TNF\text{-}\alpha^+$, (D) $CD4^+IFN\text{-}\gamma^+$, (E) $CD4^+IL\text{-}17a^+$, and (F) $CD4^+CD25^+Foxp3^+$ T cells of total $CD4^+$ T cells in the gum of mice treated with TNPs for 15 days by flow cytometric analysis (n = 6, one-way ANOVA with Tukey test).

(G) Representative 3D micro-CT images (from the buccal side) of the maxillary molar area harvested from mice after TNP treatment at day 16. Scale bar: 1 mm. The upper and lower red dashed lines represent CEJ and ABC, respectively.

(H) Representative TRAP staining images of tissue sections from mice treated with TNPs. Scale bar: 10 μm. G, B, and T refer to gingiva, bone area, and tooth, respectively.

(I) Typical H&E-stained sections of periodontal tissue after TNP treatment. Scale bar: 10 μm.

(J) Representative TNF-α immunohistochemical staining sections from tissue around ligature areas of the mice. Scale bar: 5 μm.

(K) Average distance of ABC to CEJ determined from M1 and M2 (the maxillary first molar and second molar) (n = 6, one-way ANOVA with Tukey test).

(L) Numbers of $TRAP^+$ cells in the above tissue sections (n = 5, one-way ANOVA with Tukey test).

(M) Quantitative analysis of $TNF\text{-}\alpha^+$ cells in the tissue sections (n = 5, one-way ANOVA with Tukey test). Error bars represent ±SD. *$p < 0.05$, **$p < 0.01$, ***$p < 0.001$, ****$p < 0.0001$. NS, no significance.

PBS and Treg cells were used as controls. After various treatments for 15 days, the immunosuppressive function of TNPs in the periodontal microenvironment was evaluated by cytometric analysis of cells harvested from gum tissue and CLNs. Analysis of gum cells revealed that TNPs robustly reduced the fractions of TNF-α-producing $CD4^+$ T cells (Figures 5C and S18A), $CD4^+IFN\text{-}\gamma^+$ T cells (Figures 5D and S18B), interleukin (IL)-17a-secreting $CD4^+$ cells (Figures 5E and S18C) as well as the percentage of $CD4^+CD25^+Foxp3^+$ Treg population (Figures 5F and S18D) in comparison with the PBS group. However, gum samples from mice treated with TNPs exhibited higher proportions of these $CD4^+$ subpopulations relative to naive mice. Analysis of CLNs showed that TNPs significantly reduced the fraction of $CD4^+IFN\text{-}\gamma^+$ and $CD4^+IL\text{-}17a^+$ T cells relative to the PBS group, while there was a slight difference in $CD4^+TNF\text{-}\alpha^+$ and $CD4^+CD25^+Foxp3^+$ T cells among all groups (Figure S19). It is worth mentioning that in both the gum tissue and draining CLNs, Treg cells enhanced the fraction of $CD4^+CD25^+Foxp3^+$ Treg population, and significantly decreased the fraction of $CD4^+IL\text{-}17a^+$ T cells compared with the PBS control (Figures S20A–S20H). Interestingly, TNPs exhibited superior performance over Treg cells in inhibiting $CD4^+IL\text{-}17a^+$ T cells, a pivotal $CD4^+$ T cell population that deteriorates chronic inflammation and alveolar bone resorption.[46] These results suggested that TNPs had strong potential for mitigating immune responses in the gum and CLNs of mice. To assess the efficacy of TNPs in ameliorating bone resorption, the molar area of maxillae was harvested from mice and scanned by micro-computed tomography (micro-CT). Representative three-dimensional (3D) micro-CT views from both the buccal side (Figure 5G) and lingual side (Figure S21A), as well as coronal two-dimensional (2D) view (Figure S21B), showed severe alveolar bone loss around the first molar (M1) and the second molar (M2) in the PBS group, suggesting the successful establishment of the advanced periodontitis model. Meanwhile, mice treated with TNPs had conspicuously higher alveolar bone levels compared with both control groups. Measurements of the distance between the alveolar bone crest (ABC) and cementoenamel junction (CEJ), an indicator of alveolar bone resorption,[47] consistently confirmed that TNPs substantially inhibited alveolar bone loss (Figure 5K). The negligible benefit of local injection of Treg cells to periodontal bone resorption (Figures S20I–S20J) suggested their ineffectiveness in the management of periodontitis given that alveolar bone resorption is recognized as a clinical diagnostic standard for the development and progression of periodontitis.[48] This might be because, under the periodontitis microenvironment presenting various inflammatory cytokines, such as IL-6, IL-1β, and TNF-α, locally administered Treg cells could turn into Th17 cells, which are critically responsible for bone resorption.[49–51] In addition, maxillae were sectioned for histological

analysis. Regarding osteoclast activity, representative TRAP staining images (Figure 5H) and quantitative analysis of TRAP$^+$ cells (Figure 5L) displayed similar trends: TNP treatment led to a marked decrease in the number of TRAP$^+$ osteoclasts after periodontitis development. These results verified the striking ability of TNPs to hamper osteoclast activation and rescue bone loss in periodontitis. Following hematoxylin and eosin (H&E) staining, tissue sections from the PBS group showed gum tissue destruction, disorder of periodontal tissue fibers, and attachment loss as well as evident bone resorption (Figure 5I). These were in stark contrast to the amelioration of tissue damage, reduced bone resorption, and limited attachment loss in sections from the TNP group. As shown in Figures 5J and 5M, the TNP group presented a limited stained area of TNF-α^+ cells in the gum, whereas many diffuse cells were observed in the sections of gum tissue from the PBS group. Gene expression analysis of the gum tissue indicated that inflammation-related genes, including IL-1β, IL-6, TNF-α, IFN-γ, and matrix metalloproteinase-8 (MMP-8), as well as osteoclast-related genes such as monocyte chemoattractant protein-1 (MCP-1) and RANKL, were significantly upregulated in PBS-treated mice, while the administration of TNPs dramatically decreased the expression of these genes (Figure S22).

We further evaluated the immune-modulatory capacity and tissue-protective efficacy of TNPs in a mouse model of early periodontitis (Figures S23–S28). After local TNP treatment of mice with early periodontitis (Figure S23A), the flow cytometric analysis of the CD4$^+$ T cell subpopulation in gum displayed similar results: the fractions of CD4$^+$TNF-α^+ (Figures S23B and S24A), CD4$^+$IFN-γ^+ (Figures S23C and S24B), CD4$^+$IL-17a$^+$ (Figures S23D and S24C), and CD4$^+$CD25$^+$Foxp3$^+$ cells (Figures S23E and S24D) were consistently notably lower in the TNP group relative to the PBS group. Analysis of the CD4$^+$ T cell responses in CLNs yielded results comparable with those of advanced-stage periodontitis (Figure S25). As visualized from H&E-staining images (Figure S23F), mitigated soft tissue damage and reduced bone resorption were observed in mice that received TNP treatment. Micro-CT observations (Figure S26A) and quantitative bone resorption analysis (Figure S23G) reveal that PBS-treated mice experienced moderate alveolar bone loss, indicating the development of early-stage periodontitis.[47] As expected, TNP treatment potently hindered the progression of bone resorption. TRAP staining (Figure S26B) and quantitative analysis (Figure S23H) of the tissue sections accordingly showed that TNPs suppressed TRAP$^+$ osteoclast activity near bone resorption frontier sites. Furthermore, although mice in the PBS group possessed numerous TNF-α^+ cells, TNP administration effectively limited the infiltration of these inflammatory cells to periodontitis sites (Figures S23I and S26C). In addition, the expression of inflammation- and osteoclast-related genes in gum tissue sections from the TNP group was downregulated significantly relative to the PBS group (Figure S27).

Immunoregulation mediated by TNPs in a preclinical canine model of periodontitis

A preclinical canine model of ligature-induced periodontitis was established to evaluate the effect of TNPs on the mitigation of periodontal inflammation and bone resorption. Periodontitis was induced in the left mandibles and maxillae of beagle dogs by ligature placement around the tooth cervix for 8 weeks. After the development of periodontitis, dogs were treated with PBS, conventional clinical management of periodontitis (plaque debridement and local chlorhexidine irrigation, designated as ''De/ir'' group), or TNPs (Table S3; Figures S1B and 6A). To determine periodontal status and inflammation level, a set of clinical periodontal examinations, including plaque index (PI), sulcus bleeding index (SBI), periodontal pocket depth (PPD), and clinical attachment loss (CAL), were performed at week 0 (as baseline)

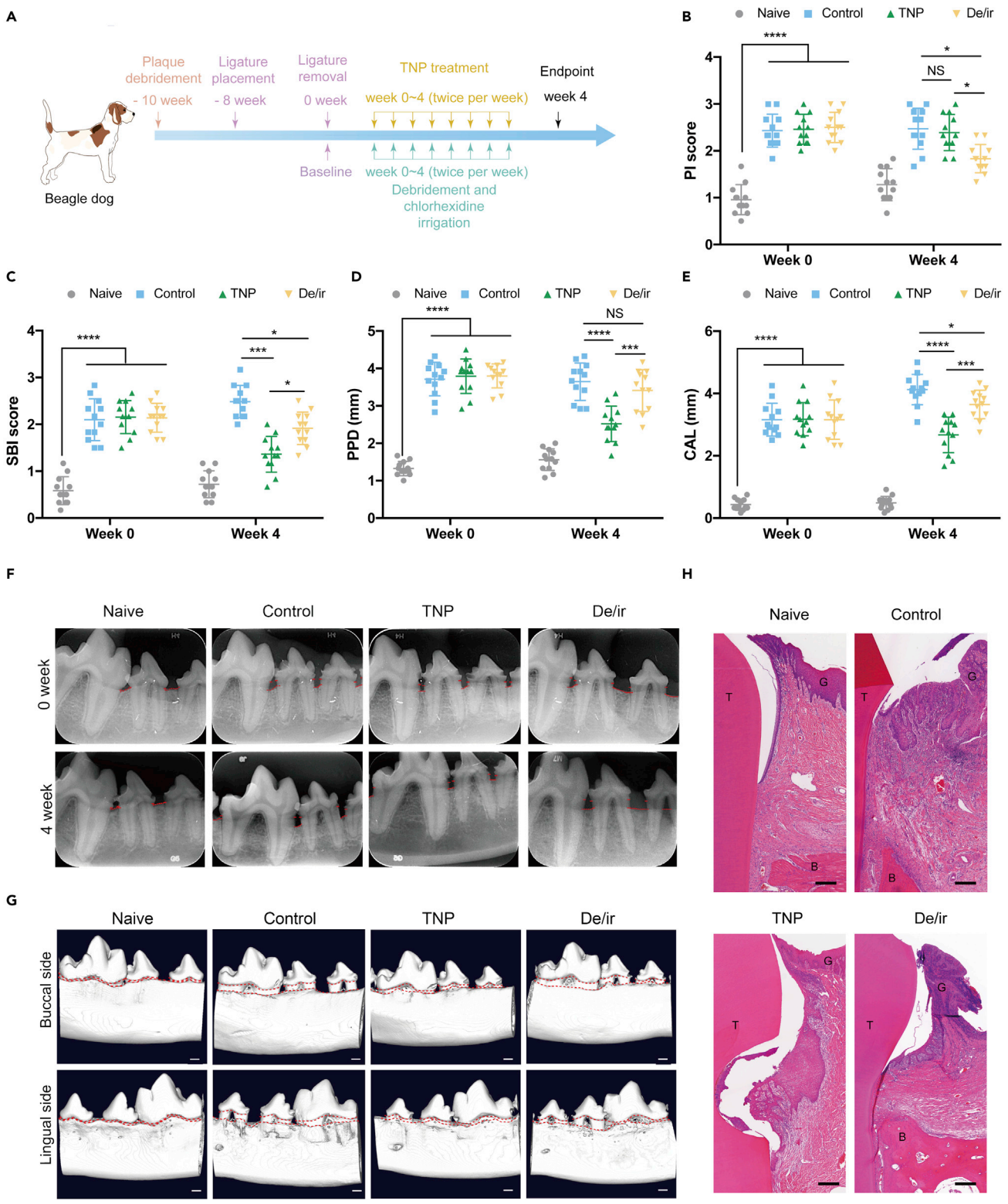

Figure 6. TNPs ameliorate progression of inflammation and diminish alveolar bone resorption in a preclinical canine model of periodontitis

(A) Experimental design for the treatment regimen of TNPs and clinical debridement and chlorhexidine irrigation in a canine model of chronic periodontitis induced by ligature placement for 8 weeks. Beagle dogs treated with PBS were used as a control.

Figure 6. *Continued*

(B–E) Clinical periodontal parameters including (B) PI, (C) SBI, (D) PPD, and (E) CAL of molar or premolar sites in dogs under different treatment conditions as measured at week 0 and 4 (12 teeth per group, Kruskal-Wallis test and one-way ANOVA with Tukey test).

(F) Representative radiographs from mandibular ligature sites of different groups obtained at weeks 0 and 4. The upper red-lined segments and lower dashed lines indicate the CEJ and ABC levels, respectively.

(G) Typical 3D micro-CT images from the buccal and lingual sides of the mandibular ligature area harvested from dogs at week 4. Scale bar: 3 mm. The upper and lower red dashed lines separately refer to the CEJ and ABC levels, respectively.

(H) Representative H&E-stained sections of tissue around ligature regions in dogs after different treatments. Scale bar: 250 μm.

G, B, and T refer to gingiva, bone area, and tooth, respectively. All data plotted as mean ± SD. *$p < 0.05$, ***$p < 0.001$, ****$p < 0.0001$. NS, no significance.

and week 4 after treatment. Baseline values (at week 0) of these periodontal parameters in dogs treated with PBS, De/ir, and TNPs showed no significant difference but were remarkably higher than those in healthy naive dogs (Figures 6B–6E). As expected, the De/ir group exhibited a much lower PI score than the other groups at week 4 (Figure 6B), indicating robust control over plaque colonization on teeth. The scores of SBI (Figure 6C), PPD (Figure 6D), and CAL (Figure 6E) in TNP and De/ir groups were markedly lower than those of the PBS group at week 4. Notably, TNPs demonstrated superior performance in reducing all these parameters compared with De/ir treatment. Clinical examinations suggested that both TNP and De/ir were efficacious in ameliorating the severity of tissue inflammation and tissue damage, but TNP treatment exhibited superior performance in recovering periodontal health. The variation of alveolar bone level was also detected via periapical radiographs at week 0 (baseline) and week 4 (Figure 6F). After periodontitis induction, dogs in PBS group, De/ir group, and TNP group displayed a similar radiographic alveolar bone level at week 0, which was conspicuously lower compared with that of naive dogs, suggesting the development of periodontitis.[52] At week 4, dogs administered TNPs showed bone levels comparable with baseline, which was in stark contrast with the progression of bone resorption in both the PBS and De/ir groups. After euthanasia of the dogs, the maxillae and mandible of dogs were harvested and scanned by micro-CT. Representative 3D micro-CT views from both buccal and lingual sides demonstrated that TNP-treated dogs presented remarkably less alveolar bone resorption compared with dogs treated with PBS and De/ir (Figure 6G). Quantitative analysis of ABC-CEJ distance further corroborated that TNP treatment promoted greater suppression of bone loss than PBS ($p < 0.001$) or De/ir ($p < 0.01$) treatments (Figure S29). Notably, De/ir treatment showed no apparent advantage in controlling bone resorption over the PBS group. TRAP staining of tissue sections further confirmed that TNPs effectively inhibited osteoclast activity at alveolar bone around ligature sites (Figure S30). Histological differences in the periodontium among these groups were observed from H&E-stained sections (Figure 6H). Compared with the periodontium of naive dogs, the PBS group exhibited more serious attachment loss and ulcerous lesions in periodontal tissue, including gingival tissue loss, irregular arrangements of gingival tissue fibers, as well as severe and widespread inflammatory cell infiltration. In contrast, the treated groups exhibited fewer ulcerous phenomena and attachment loss. TNP-treated dogs distinctly outperformed the De/ir group in restricting inflammation as well as mitigating gingival damage and attachment loss. Gene expression evaluation in gum tissue revealed that inflammation-related genes, including IL-1β, IL-6, IL-17a, and osteoclast-related gene RANKL, were obviously upregulated in both the PBS and De/ir groups, whereas TNP-treated dogs presented remarkably lower expression of these genes (Figure S31). Taken together, our findings provided robust evidence that TNPs alleviated inflammatory responses and alveolar bone resorption in a preclinical canine model of periodontitis, suggesting them as an alternative to manage chronic periodontitis and highlighting their potential for further clinical translation.

Conclusion

In summary, we report a biomimetic immunomodulatory strategy based on nanoparticulate Treg cells for manipulating the overactive immune microenvironment. Artificial nanoscale cells decorated with intrinsic membrane proteins and function to suppress multiple overactive immune cells have been fabricated by coating nanoparticulate substrates with Treg cell membranes. This Treg cell biomimicry approach confers NPs with multifaceted immunosuppressive capabilities through direct crosstalk with target cells, including macrophages, DCs, and effector T cells, which correspondingly inhibits the osteoclastogenesis of macrophages, the maturation of DCs, and the function of effector T cells. Coated NPs exhibit multiple functions, including curtailing hyperactive immune responses to ameliorate inflammation in periodontal lesions and rescuing inflammatory alveolar bone loss in both murine and preclinical canine models of periodontitis. Different from Treg cells, artificial nanoparticulate Treg cells are less sensitive to the complex inflammatory microenvironment and able to maintain the immunosuppressive capacity to regulate immuno-inflammatory responses and to protect inflamed tissues. Furthermore, their viable storability and transportability offer great potential for future translation. In addition, personalized medicine could be pursued by exploiting customized Treg cell membranes, which may also remarkably reduce immunogenicity. A range of diseases, such as arthritis, inflammatory bowel disease, graft-versus-host disease, type 1 diabetes mellitus, and systemic lupus erythematosus, suffer from excessive immune activation.[2,7,46] Given the regulatory role of Treg cells in maintaining the homeostasis of the immune system, we anticipate that NP-based biomimetic immunoregulation would become a universal platform for manipulating the dysregulated immune microenvironment, particularly in these diseases caused by immune system disorders. Regarding further translation of these nanoparticulate Treg cells, a few challenges need to be tackled in the future. To boost immunotherapeutic outcomes, drug payloads could be integrated into the platform and comprehensive optimization of dosages is required to ensure safety and efficacy. Meanwhile, targeting ability of these NPs would be necessary, particularly for application in systemic administration. In addition, purification procedures and the scale-up issue regarding source cells and TNPs both entail further endeavors.

EXPERIMENTAL PROCEDURES

Resource availability

Lead contact

Further information and requests for materials should be directed to and will be fulfilled by the lead contact, Jinyao Liu, jyliu@sjtu.edu.cn.

Materials availability

The materials generated in this study are available from the corresponding author upon request.

Data and code availability

The data used to support the findings of this study are available from the corresponding author upon request.

Animals

C57BL/6 mice were provided by and bred under specific pathogen-free (SPF) conditions in the Animal Center at Renji Hospital. Eight- to 10-week-old female mice were used for all murine experiments. Male beagle dogs (12–18 months) were used for therapeutic experiments. All animal experiments were carried out according to

ethical guidelines and approved by the Institutional Animal Care and Use Committee of Shanghai Jiao Tong University School of Medicine.

Isolation and expansion of Treg cells

Murine $CD4^+CD25^+$ Treg cells were purified from the splenocytes of female C57BL/6 mice via the MACS system (Miltenyi Biotec). Briefly, ~1 × 10^8 mouse splenocytes were first subjected to indirect magnetic labeling of non-$CD4^+$ T cells with biotin-antibody cocktail and anti-biotin microbeads, labeling of $CD25^+$ cells with CD25-PE, and subsequent magnetic separation. Then the $CD4^+CD25^+$ cells were enriched via positive magnetic selection after labeling of $CD25^+$ cells with anti-PE microbeads. Approximately 1.6 × 10^6 $CD4^+CD25^+$ Treg cells were enriched from these splenocytes and exhibited a purity of at least 92% as analyzed by flow cytometry. Afterward, the obtained Treg cells were seeded in a 24-well plate at 2.5×10^5 cells per well (Costar) and stimulated with anti-CD3/anti-CD28-coated microbeads (Miltenyi Biotec) at a cell-to-bead ratio of 1:3 in Dulbecco's modified eagle's medium (Hyclone) supplemented with 10% fetal bovine serum (FBS, Invitrogen), 1% penicillin/streptomycin (Invitrogen), 50 μM β-mercaptoethanol, 2 mM L-glutamine, IL-2 (200 U/mL, R&D Systems) for 9 days with culture medium refreshed every 2 days. Then cells were subjected to re-stimulation with fresh beads at a ratio of 1:1. On day 14, the beads were removed from the cells using a MACSiMAG Separator (Miltenyi Biotec) and the cell counting indicated a ~16-fold of expansion. The phenotype of expanded $CD4^+CD25^+$ Treg cells was analyzed by flow cytometry with cell surface staining using CD4-fluorescein isothiocyanate (FITC) (BioLegend), CD25-PE (BioLegend), and intracellular staining using Foxp3-APC (BioLegend) and Foxp3 staining buffer set (eBioscience). To collect canine Treg cells, peripheral blood mononuclear cells (PBMCs) were first isolated from fresh peripheral blood from beagle dogs by density gradient centrifugation over Ficoll/Paque (GE Healthcare). The obtained PBMCs were stained with FITC-conjugated anti-CD4 (eBioscience) and APC-labeled anti-CD25 antibodies (eBioscience) and sorted by flow cytometry via BD FACSAria III cell sorter (BD Biosciences), yielding a purity of at least 98%. As for canine Treg cell yield, approximately 4 × 10^6 $CD4^+CD25^+$ cells were obtained from 10 mL of peripheral blood. The phenotype of the sorted cells was similarly determined using flow cytometric analysis of CD4-FITC (eBioscience), CD25-APC (eBioscience), and Foxp3-PE (eBioscience).

Cell membrane collection

Membranes of Treg cells were collected as previously described with slight modifications.[31] Briefly, Treg cells were suspended in hypotonic lysis buffer supplemented with protease and phosphatase inhibitor cocktail (Thermo Fisher Scientific), 30 mM Tris/HCl, 75 mM sucrose, 0.2 mM EDTA (the above components from Sigma-Aldrich), and incubated on ice for 30 min. Then the cell suspension was carefully ground and homogenized using a Dounce homogenizer with a tight-fitting pestle (30 passes), followed by centrifugation at 800 × *g* for 5 min at 4°C to discard the large debris and cell nuclei. The supernatant was subsequently centrifuged at 3,200 × *g* for 5 min at 4°C to collect supernatant. Meanwhile the obtained pellet was resuspended in hypotonic lysis buffer, and the homogenization/centrifugation process was repeated another three times until thorough lysis of the cells was determined by light microscopy. Lastly, the pooled supernatant was centrifuged at 21,000× *g* for 35 min at 4°C. The supernatant was discarded and the pellet was collected. For purification, the cell membrane pellet was washed twice with PBS to remove intracellular proteins and small organelles. The membrane protein concentration was detected using a BCA kit (Beyotime). Approximately 150 million mouse Treg cells or 110 million canine Treg cells yielded 1 mg of membrane material

(protein weight). The murine and canine Treg cell membranes were suspended in PBS containing 0.2 mM EDTA at a protein concentration of 4 mg/mL and stored at −80°C for further use.

Preparation of NPs

PLGA NPs were synthesized according to previous methods.[20] Briefly, 1 mL of PLGA (50:50) in acetone (10 mg/mL) was added dropwise into 3 mL of water under magnetic stirring. Then the solution was subjected to rotary evaporation until the complete evaporation of acetone. For fluorescent imaging assays, 2 μL of 1,1′-dioctadecyl-3,3,3′,3′-tetramethylindodicarbocyanine, 4-chlorobenzenesulfonate salt (DiD) in ethanol (1 mg/mL, Thermo Fisher Scientific) was added to PLGA acetone solution prior to PLGA NP synthesis. For cell membrane coating to prepare TNPs, the harvested Treg plasma membranes were mixed with the PLGA cores at a membrane protein-to-polymer weight ratio of 1:1. The mixture was extruded 11 times through polycarbonate membranes (400 nm and 200 nm) using a mini-extruder (Avanti). The as-synthesized NPs were resuspended in PBS for further experiments. The murine and canine TNPs were suspended in PBS containing 0.2 mM EDTA (2 mg/mL) and stored at −80°C for further use.

Characterization of NPs

TNPs were stained with uranyl acetate (1 wt %) and imaged with TEM (HT7700, HITACHI) to assess morphology. Cyro-TEM observation for TNPs was conducted as previously described.[53] A volume of 10 μL of TNP sample was applied to lacey carbon grids (Ted Pella, 01824G) that were coated with 2–3-nm-thick continuous carbon film and glow discharged with air using the Pelco easiGlowTM System. The grids were blotted for 3 s at 4°C, plunged into liquid ethane by an FEI Vitroblot Mark IV at 100% humidity, and loaded onto a Talos Arctica G2 transmission electron microscope operated at 200 kV for data collection. Images were recorded by a Falcon 3 camera.

Hydrodynamic size and surface zeta potential of TNPs were assessed with DLS (Zetasizer, Malvern) for further validation of the successful coating of cell membrane onto polymeric cores. To detect specific surface markers on TNPs, samples of Treg lysate, Treg vesicles, and TNPs were examined via western blot. For sample preparation, TNPs and Treg vesicles were prepared at a protein concentration of 2 mg/mL in 60 μL of lithium dodecyl sulfate (LDS) sample loading buffer (Invitrogen) and 1.8×10^7 Treg cells with equal amount of membrane proteins were suspended in 60 μL of LDS buffer, followed by sample heating at 70°C for 30 min. Then 20 μL of each sample was used for SDS-PAGE electrophoresis at 150 V for ~1 h using 4%–12% Bolt Bis-Tris Plus gels in Bolt MES running buffer (Invitrogen). The protein-transferred polyvinyl difluoride (PVDF) membranes (Millipore) were then incubated with primary antibodies: rabbit anti-mouse CTLA-4 (Abcam), LAG3 (Cell Signaling Technology [CST]), CD39 (CST), CD73 (CST), and CD27 (Abcam), followed by incubation with horseradish peroxidase (HRP)-conjugated anti-rabbit IgG secondary antibody (Beyotime). The PVDF membranes were then incubated with enhanced chemiluminescence (ECL) substrate (Thermo Scientific) and exposed in an Odyssey infrared imaging system (LI-COR) for protein band observation.

Flow cytometric analysis was conducted to verify the outward orientation of surface proteins on TNPs. TNPs (0.1 mg/mL, suspended in 100 μL of staining buffer) and 1.5×10^6 Treg cells with equal amount of membrane proteins (suspended in 100 μL of staining buffer) were incubated with PE-labeled CTLA-4 antibody (diluted at 1:100, BioLegend) at 4°C for 30 min. After PBS rinse by centrifugation

at 21,000 × *g* for 30 min at 4°C three times, samples were resuspended in 100 μL of PBS for flow cytometric analysis.

Cell culture

All cells were cultured in medium supplemented with 10% FBS, 1% penicillin/streptomycin, 2 mM L-glutamine, 1 mM sodium pyruvate, 0.1 mM non-essential amino acids, and 10 mM HEPES at 37°C in a humidified environment with 5% CO_2.

Adhesion assay of TNPs

Chamber slides (Thermo Fisher Scientific) were first coated with poly-L-lysine (1 mg/mL, Sigma-Aldrich) at room temperature (RT) for 15 min and washed twice. Then 1 mL of macrophage (2×10^6 per well) and splenocyte (4×10^6 per well) suspensions were seeded onto the dishes and incubated with 100 μL of 0.2 mg/mL DiD-labeled TNPs and NPs (equivalent concentration to that of TNPs as quantified via fluorescence intensity) at 4°C for 1 h to block cellular uptake of NPs. Afterward, the slides were washed with PBS three times and fixed with 4% paraformaldehyde (PFA) at 4°C for 20 min. Subsequent procedures for various cell cultures were as follows: macrophage cocultures were stained with Hoechst 33342 and Neuro-DiO, while splenocyte cocultures were incubated with 3% BSA (Sigma-Aldrich) for 30 min for blocking of nonspecific binding sites and subsequently stained with FITC-labeled CD3 (BioLegend) and Hoechst 33342, followed by PBS washes and visualization under confocal microscopy (Leica TSC SP8). For further analysis of targeted adhesion capacity of TNPs onto macrophages, DCs, and T cells, TNPs and NPs were similarly incubated with these cells in 48-well plates at 4°C for 1 h. Then macrophage culture was stained with CD11b-FITC (BioLegend), DC culture was stained with CD11c-FITC (BioLegend), and splenocyte culture was stained with CD3-FITC (BioLegend). These cell cultures were subsequently analyzed via flow cytometry for the medium fluorescence intensity of the bound TNPs and NPs.

In vitro macrophage-osteoclast differentiation

For osteoclast-related assays, bone marrow cells were isolated by flushing the bone marrow of tibiae and femurs of naive C57BL/6 mice with culture medium (α-Minimum Essential Medium [MEM] containing 10% FBS and 1% penicillin/streptomycin) and seeded in plates overnight, followed by collecting the non-adherent bone marrow monocytes (BMMs). After washing, BMMs were cultured in the above medium supplemented with 30 ng/mL MCSF (Peprotech) for purification and expansion for further use. For *in vitro* osteoclast differentiation assay, macrophage suspensions were seeded in flat-bottomed 96-well plates (1×10^4 per well) in culture medium supplemented with MCSF (30 ng/mL, Peprotech) and RANKL (50 ng/mL, Peprotech). These cells were simultaneously treated with 20 μL of TNPs (0.2 mg/mL), NPs (equivalent concentration), and 1×10^5 Treg cells, respectively, while the untreated group served as the positive control. Five days later, TRAP staining using the leukocyte acid phosphatase kit (Lianke Biotech) was conducted on the above samples to evaluate osteoclast differentiation, in which multinucleated $TRAP^+$ (purple color) cells were identified as osteoclasts, and purple-colored cells with one or two nuclei were identified as macrophages. The number of $TRAP^+$ osteoclasts per well was further quantified. In addition, 1 mL of macrophage suspension was plated in 24-well plates (1×10^6 per well) and treated with 100 μL of TNPs (0.2 mg/mL) and NPs (equivalent concentration) in the presence of MCSF (30 ng/mL) and RANKL (50 ng/mL) for 3 days to assess the relative mRNA expression of IDO and osteoclast-related genes via qPCR. For western blot, similar osteoclast cultures treated with TNPs and NPs for 3 days were lysed to collect proteins, followed by SDS-PAGE electrophoresis, PVDF membrane transfer, incubation with monoclonal antibody against IDO (CST), and

corresponding secondary antibody. β-actin was used as an internal control. The protein band was detected by exposure in an Odyssey infrared imaging system (LI-COR).

Apoptosis assay of macrophages

A volume of 1 mL of macrophage suspension was seeded in 24-well plates (5×10^5 per well) and treated with 100 μL of TNPs (0.2 mg/mL), NPs (equivalent concentration), and 3×10^6 Treg cells (with equivalent membrane protein content to TNPs) in the presence of MCSF (30 ng/mL) and RANKL (50 ng/mL) for 24 h. Then the cells were stained with annexin V-FITC and propidium iodide solution (both from BD Biosciences) for 15 min at RT in the dark and immediately analyzed by flow cytometry. The percentage of annexin V-positive cells was calculated to assess the apoptosis rate. Furthermore, in order to ascertain that the inhibitory effects of TNPs exerted on macrophages was attributable to the participation of CD80/86 molecules, neutralization antibodies of CD80 and CD86 (10 μg/mL, both from R&D Systems) were added into the cell culture for 24 h for CD80/CD86 blocking, followed by the similar treatment with TNPs for another 24 h and collection for the apoptosis assay mentioned above.

Flow cytometry

Cells were washed with PBS, incubated with murine anti-CD16/CD32 (BioLegend) for 15 min at RT to block FcγR, and fixed with viability stain 780 (BD Biosciences) for 15 min at RT to exclude dead cells. Then the surface of cells was stained with fluorochrome-conjugated antibodies in staining buffer (eBioscience) at 4°C for 30 min in the dark. As for intracellular staining, cells were fixed, permeabilized, and stained with fluorochrome-labeled antibodies. The collected cells were then analyzed by flow cytometry (CytoFLEX, Beckman Coulter) and statistically analyzed using FlowJo software.

qPCR analysis

For real-time qPCR, RNA was isolated from various cells or murine gum tissue using TRIzol (Invitrogen). Complementary DNA (cDNA) was synthesized using the transcriptor first-strand cDNA synthesis kit (Roche) according to the manufacturer's instructions. The obtained cDNA was amplified via real-time qPCR using FastStart Essential DNA Green Master (Roche) on LightCycler 480 (Roche). The cDNA expression levels were normalized to the housekeeping gene GAPDH. The primer sequences are listed in Table S4.

Isolation and induction of DCs

DCs were harvested by inducing bone marrow cells isolated from femurs and tibiae of naive C57BL/6 mice in DMEM (Hyclone) supplemented with 10% FBS, 50 μM 2-mercaptoethanol (ME), 1% penicillin-streptomycin, and recombinant granulocyte-macrophage colony stimulating factor (GM-CSF, 20 ng/mL, Peprotech). Culture medium was replenished on days 3 and 6, and non-adherent cells were transferred to new petri dishes to collect the purified non-adherent cells for further use.

Electron microscopy

To confirm the close contact between TNPs and DCs, poly-L-lysine-coated plates with DC-TNP coculture were fixed and processed as previously described with slight modifications.[54] Briefly, 1 mL of DC suspension (1×10^7 per well) was seeded onto poly-L-lysine-coated 24-well plates and incubated with 100 μL of TNPs (0.2 mg/mL) and NPs (equivalent concentration) at 4°C for 1 h. After PBS rinse, the samples were prefixed with 2.5% glutaraldehyde in PBS buffer for 1 h at 4°C and three washes with

PBS. Then cells were postfixed with 1% osmium tetroxide and three rinses with PBS. Next, samples were dehydrated in a graded series of ethanol and embedded in epoxy resin. The sections were cut and imaged with TEM.

Expression of surface costimulatory molecules on DCs

For analysis of the surface phenotype of DCs, 1 mL of DC suspension (1×10^6 per well) was seeded into 24-well plates and separately treated with 100 μL of TNPs (0.2 mg/mL), NPs (equivalent concentration), and 3×10^6 Treg cells (with equivalent membrane protein content to TNPs) in the presence of LPS (100 ng/mL) for 48 h. After PBS rinse, cells were stained with CD11c-FITC, CD80-PE, CD86-APC, and CD70-PE antibodies (all from BioLegend) at 4°C for 30 min. Then the washed cell cultures were subjected to flow cytometric analysis of the expression of these surface ligands on CD11c-gated populations. To further assess the expression of these costimulatory molecules in treated DCs on the mRNA level, the cocultures were subjected to RNA extraction and qPCR analysis.

Immunofluorescence staining of DC-TNP coculture

To observe the interaction between TNPs and the co-stimulation ligands CD80 and CD86 on DCs, 100 μL of DiD-labeled TNPs (0.2 mg/mL) was incubated with 1 mL of DC suspension seeded on poly-L-lysine-coated chamber slides (2×10^6 per well) at 4°C for 1 h. Then samples were fixed and rinsed, followed by blocking with 3% BSA (Sigma-Aldrich) for 30 min at RT. After PBS rinse, DCs were stained with PE-conjugated CD80 antibody (BioLegend), FITC-conjugated CD86 antibody (BioLegend), and Hoechst. The samples were dried and mounted prior to confocal imaging. For the quantitative analysis of the colocalization between TNPs and CD80 or CD86 on DCs, Mander colocalization coefficient between the fluorescence signals of TNPs and CD80 or CD86 was calculated using ImageJ with Coloc2 plugin, respectively. A total of 10 images were analyzed for both groups. MCC refers to a metric between 0 and 1, where 0 indicates no colocalization and >0.5 indicates colocalization. The MCC value is closer to 1 if the two fluorescent signals are highly co-localized.

In vitro T cell proliferation and activation assay

For the functional assay of naive T cells, splenic cells isolated from naive C57BL/6 mice were seeded in flat-bottomed 96-well plates (1×10^6 per well, 200-μL suspension) and activated with plate-bound anti-CD3 (1.5 μg/mL, BD Biosciences), soluble anti-CD28 (1 μg/mL, BD Biosciences) and IL-2 (200 U/mL) for 4 days; meanwhile 20 μL of TNPs (0.2 mg/mL), NPs (equal concentration), and 6×10^5 Treg cells (with equivalent membrane protein content to TNPs) were added to the cell cultures and replenished every other day considering NP consumption by cells. For the examination of the proliferation activity of T cells, the splenic cells were labeled with CFSE (5 μM, Invitrogen) before the above-mentioned treatments. After different treatments, the cells were collected, washed, and stained with CD3-BV650 antibody (BD Biosciences), CD4-PerCP-Cy5.5, and CD8-APC antibodies, followed by intracellular staining of Ki67-FITC, TNF-α-PE, and IFN-γ-PE-Cy7 antibodies (BioLegend) for flow cytometric analysis. The fractions of CFSE dilution, $Ki67^+$ cells, and $TNF\text{-}\alpha^+/IFN\text{-}\gamma^+$ cells in both $CD3^+CD4^+$ and $CD3^+CD8^+$ subsets were assessed to evaluate the proliferation and activation of naive T cells, respectively.

Treatment with TNPs in murine and canine models of periodontitis

All animal procedures were approved by the Institutional Animal Care and Use Committee of Shanghai Jiao Tong University School of Medicine. For murine models of early and advanced periodontitis, female C57BL/6 mice 8–10 weeks old were used for periodontitis induction by ligature placement around molars as described

previously.[47] Briefly, silk sutures (8-0, Jinhuan) were inserted into the subgingival area of M1 of mice for 10 days and 30 days for the induction of early-stage and advanced-stage periodontitis, respectively. The ligation was checked once a week and was renewed in case of loosening or displacement. After the establishment of the two periodontitis models as determined by alveolar bone resorption level of the treated side of maxillae, the ligatures were removed, and the mice were used to study the beneficial effects of TNPs. For early periodontitis, 20 μL of mouse TNPs (2 mg/mL) was injected into the gingival tissue at the proximal side of M1, the distal side of M2, and the interdental site between M1 and M2 on days 1, 3, 5, 7, 9, 11, 13, and 15 after the removal of ligatures. Sterile PBS was injected according to a similar regime as a negative control, and naive mice were bred as a healthy control group. For advanced periodontitis, 20 μL of mouse TNPs (2 mg/mL) was similarly administered to the gingiva with the same dosing frequency for 15 days. The PBS-treated group and naive group were also adopted as negative controls and healthy controls, respectively. Establishment of the periodontitis model and treatment process for mice was all performed under a binocular loupe. The canine model of periodontitis was established in eight male beagle dogs (12–18 months old), which were then used in treatment experiments of canine TNPs. Ligature-induced periodontitis in beagle dogs was induced as previously depicted.[52] For the preparation and maintenance of healthy periodontal tissue, all dogs received dental plaque debridement using sterilized dental Gracey curettes (Hu-Friedy) and were given a hard pellet diet for 2 weeks. Afterward, periodontitis was induced in six of the dogs on the left mandibular third premolar (PM3), fourth premolar (PM4), and M1, as well as the left maxillary PM2, PM3, and PM4 by placing 2-0 silk sutures around the cervix of these teeth. To stabilize the ligation, shallow notches were created at the proximal and distal sides of tooth cervix using a round bur, and a dental composite resin was added around the ligatures. Soft-moistened diet was provided for the following 8 weeks to increase plaque formation. Ligatures were checked weekly, and those loosened or lost were immediately repaired. After the periodontitis-induction phase, the dogs were randomly divided into three groups: TNP group (n = 2, 12 teeth) was injected with 50 μL of canine TNPs (2 mg/mL) into the gingiva of each tooth at the proximal side and the distal side; control group (n = 2, 12 teeth) received sterile PBS treatment in a similar manner and was taken as the negative control; and the De/ir group (n = 2, 12 teeth) received conventional clinical management for periodontitis (dental plaque debridement and chlorhexidine irrigation in the periodontal pocket), serving as the positive control. The above-mentioned treatments were all given twice a week over a 4-week-period for the therapeutic efficacy study. The two remaining dogs (n = 2, 12 teeth) that were not induced for periodontitis received dental plaque scaling before the therapeutic experiments for the other groups and then served as the healthy control group (designated the naive group) during treatments.

Clinical periodontal examination and radiographic analysis

After dental ligature removal (week 0, baseline), clinical periodontal parameters including PI, SBI, PPD, and CAL were examined utilizing a sterilized periodontal probe (Hu-Friedy) to evaluate inflammation and tissue damage in the periodontium (Table S5). Meanwhile, standardized periapical radiographs were also taken to assess any change in alveolar bone level as indicated by the distance between CEJ (as a reference landmark on the tooth) and the marginal bone level. Clinical periodontal status and radiographic analysis were re-evaluated for all dogs after 4 weeks of various treatments, followed by the euthanasia of all dogs for tissue biopsy. All periodontal parameter measurements were conducted in a blinded manner by the same experienced clinician.

Evaluation of local immuno-inflammatory responses in murine and canine models

For murine investigations, mice were sacrificed and the gingival tissue around M1 and M2 was carefully separated from the maxillae and cut into 1-mm^3 pieces. A single-cell suspension was obtained via an enzymatic dissociation procedure using collagenase IV, Dispase II, and DNase I at 37°C for 3 h, followed by 70-μm filtering to collect the suspension. The draining CLNs were also harvested, homogenized in buffer for flow cytometry (eBioscience), and filtered to collect the single-cell suspensions. For intracellular cytokine analysis, the above cells were initially stimulated with leukocyte activation cocktail (BD Biosciences) for 5 h prior to FcγR blocking, viability staining, and surface staining with antibodies against CD3-FITC, CD4-PerCP-Cy5.5, and CD25-PE (all from BioLegend). Then the cells were fixed, permeabilized, and stained with antibodies to IL-17a-APC, TNF-α-PE, IFN-γ-PE-Cy7, and Foxp3-APC for flow cytometric analysis. Cells were first gated on forward scatter (FSC)/side scatter (SSC). Singlet cells were then gated using FSC-A and FSC-H. Further gating was conducted on singlet cells. $CD4^+$ T cells were gated on the viable $CD3^+$ population. The fractions of TNF-α^+, IFN-γ^+, IL-17a^+, and $CD25^+Foxp3^+$ populations were calculated on total $CD4^+$ T cells.

After biopsy, the murine and canine gum tissues surrounding the treated teeth were immediately harvested and stored at −80°C for RNA extraction. The cDNA was synthesized and used for real-time qPCR to analyze the gene expression in gum tissue. The primers are listed in Table S6.

Micro-CT analysis

To assess the extent of alveolar bone resorption, the resected murine maxillae were fixed in 4% PFA for 24 h, while the harvested maxillae and mandibles of dogs were fixed for 48 h, followed by micro-CT scanning (PerkinElmer). The 3D views from the buccal side and the lingual side were reconstructed and the 2D view was generated via the accompanying software. Based on the 3D images, the distance from the CEJ to the ABC was measured at six sites for each tooth, including mesial, distal, and middle points of both buccal and lingual sides using ImageJ. For murine analysis, the value of CEJ-ABC distance for each sample derived from the average of the sites of M1 and M2 and six samples was performed for each group. For canine analysis, quantification of ABC-CEJ distance derived from the average of each treated tooth and 12 teeth was performed for each group.

Histological analysis of murine and canine periodontium

After micro-CT analysis, the murine tissue specimens were decalcified in 10% EDTA for 15 days, while the canine samples were decalcified for 4 months, followed by embedment in paraffin. Then serial sections were cut along the mesio-distal direction, and murine and canine samples were stained with H&E and TRAP. $TRAP^+$ multinucleated cells were identified as osteoclasts and quantified via ImageJ. Immunohistochemical staining was conducted on murine sections using anti-TNF-α antibody (Abcam) and the number of TNF-α^+ cells calculated.

Statistical analysis

All data were plotted as means ± standard deviation (SD.). The statistics were analyzed using GraphPad software by unpaired two-tailed Student's t test and a one-way analysis of variance (ANOVA) with Tukey's post hoc analysis for multiple comparisons. Scoring data involved in canine clinical periodontal examination were analyzed by the Kruskal-Wallis test. Differences were considered statistically significant when $p < 0.05$ (*$p < 0.05$, **$p < 0.01$, ***$p < 0.001$, and ****$p < 0.0001$).

SUPPLEMENTAL INFORMATION

Supplemental information can be found online at https://doi.org/10.1016/j.matt.2021.08.015.

ACKNOWLEDGMENTS

This work was financially supported by the National Natural Science Foundation of China (21875135, 81570948, 52171075), the Medicine and Engineering Cross Research Foundation of Shanghai Jiao Tong University (YG2017ZD06), the Recruitment Program of Global Youth Experts of China (D1410022), the Shanghai Municipal Education Commission-Gaofeng Clinical Medicine grant support (20181704), the Innovative Research Team of High-Level Local Universities in Shanghai (SSMU-ZLCX20180701), the Youth Science and Technology Talents Yang Fan Plan of Shanghai (19YF1427800), the Program of Science and Technology Commission of Shanghai Municipality (201409006300), and the Interdisciplinary Program of Shanghai Jiao Tong University (ZH2018QNA44).

AUTHOR CONTRIBUTIONS

J.L., E.L., and W.T. supervised the project. J.L. conceived and designed the experiments with S.L. S.L., L.W., Y.G., L.L., W.Z., M.J., and C.M. performed all experiments. All authors analyzed and discussed the data. S.L. and J.L. wrote the paper. J.Z., X.H., C.C., and W.T. revised the manuscript together with S.L. and J.L.

DECLARATION OF INTERESTS

The authors declare no competing interests.

Received: February 2, 2021
Revised: July 9, 2021
Accepted: August 12, 2021
Published: September 14, 2021

REFERENCES

1. Rosenblum, M.D., Gratz, I.K., Paw, J.S., and Abbas, A.K. (2012). Treating human autoimmunity: current practice and future prospects. Sci. Transl. Med. *4*, 125sr1.

2. Perretti, M., Cooper, D., Dalli, J., and Norling, L.V. (2017). Immune resolution mechanisms in inflammatory arthritis. Nat. Rev. Rheumatol. *13*, 87–99.

3. Cekici, A., Kantarci, A., Hasturk, H., and Van Dyke, T.E. (2014). Inflammatory and immune pathways in the pathogenesis of periodontal disease. Periodontol. 2000 *64*, 57–80.

4. Kinane, D.F., Stathopoulou, P.G., and Papapanou, P.N. (2017). Periodontal diseases. Nat. Rev. Dis. Primers *3*, 17038.

5. Buckley, C.D., Gilroy, D.W., Serhan, C.N., Stockinger, B., and Tak, P.P. (2013). The resolution of inflammation. Nat. Rev. Immunol. *13*, 59–66.

6. Joffre, O., Nolte, M.A., Spörri, R., and Reis e Sousa, C. (2009). Inflammatory signals in dendritic cell activation and the induction of adaptive immunity. Immunol. Rev. *227*, 234–247.

7. Fugger, L., Jensen, L.T., and Rossjohn, J. (2020). Challenges, progress, and prospects of developing therapies to treat autoimmune diseases. Cell *181*, 63–80.

8. Shapiro, A.M., Pokrywczynska, M., and Ricordi, C. (2017). Clinical pancreatic islet transplantation. Nat. Rev. Endocrinol. *13*, 268–277.

9. Preshaw, P.M. (2018). Host modulation therapy with anti-inflammatory agents. Periodontol. 2000 *76*, 131–149.

10. Taylor, P.C., Moore, A., Vasilescu, R., Alvir, J., and Tarallo, M. (2016). A structured literature review of the burden of illness and unmet needs in patients with rheumatoid arthritis: a current perspective. Rheumatol. Int. *36*, 685–695.

11. Wong, X.Y., Sena-Torralba, A., Álvarez-Diduk, R., Muthoosamy, K., and Merkoçi, A. (2020). Nanomaterials for nanotheranostics: tuning their properties according to disease needs. ACS Nano *14*, 2585–2627.

12. Fenton, O.S., Olafson, K.N., Pillai, P.S., Mitchell, M.J., and Langer, R. (2018). Advances in biomaterials for drug delivery. Adv. Mater. *30*, e1705328.

13. McHugh, M.D., Park, J., Uhrich, R., Gao, W., Horwitz, D.A., and Fahmy, T.M. (2015). Paracrine co-delivery of TGF-β and IL-2 using CD4-targeted nanoparticles for induction and maintenance of regulatory T cells. Biomaterials *59*, 172–181.

14. Raimondo, T.M., and Mooney, D.J. (2018). Functional muscle recovery with nanoparticle-directed M2 macrophage polarization in mice. Proc. Natl. Acad. Sci. U S A *115*, 10648–10653.

15. Stabler, C.L., Li, Y., Stewart, J.M., and Keselowsky, B.G. (2019). Engineering immunomodulatory biomaterials for type 1 diabetes. Nat. Rev. Mater. *4*, 429–450.

16. Cifuentes-Rius, A., Desai, A., Yuen, D., Johnston, A.P.R., and Voelcker, N.H. (2021). Inducing immune tolerance with dendritic cell-targeting nanomedicines. Nat. Nanotechnol. *16*, 37–46.

17. Feng, X., Xu, W., Li, Z., Song, W., Ding, J., and Chen, X. (2019). Immunomodulatory nanosystems. Adv. Sci. *6*, 1900101.

18. Brusini, R., Varna, M., and Couvreur, P. (2020). Advanced nanomedicines for the treatment of inflammatory diseases. Adv. Drug Deliv. Rev. *157*, 161–178.

19. Duivenvoorden, R., Senders, M.L., van Leent, M.M.T., Pérez-Medina, C., Nahrendorf, M., Fayad, Z.A., and Mulder, W.J.M. (2019). Nanoimmunotherapy to treat ischaemic heart disease. Nat. Rev. Cardiol. *16*, 21–32.

20. Zhang, Q., Dehaini, D., Zhang, Y., Zhou, J., Chen, X., Zhang, L., Fang, R.H., Gao, W., and Zhang, L. (2018). Neutrophil membrane-coated nanoparticles inhibit synovial inflammation and alleviate joint damage in inflammatory arthritis. Nat. Nanotechnol. *13*, 1182–1190.

21. Gao, C., Huang, Q., Liu, C., Kwong, C.H.T., Yue, L., Wan, J.B., Lee, S.M.Y., and Wang, R. (2020). Treatment of atherosclerosis by macrophage-biomimetic nanoparticles via targeted pharmacotherapy and sequestration of proinflammatory cytokines. Nat. Commun. *11*, 2622.

22. Netea, M.G., Domínguez-Andrés, J., Barreiro, L.B., Chavakis, T., Divangahi, M., Fuchs, E., Joosten, L.A.B., van der Meer, J.W.M., Mhlanga, M.M., Mulder, W.J.M., et al. (2020). Defining trained immunity and its role in health and disease. Nat. Rev. Immunol. *20*, 375–388.

23. Sica, A., and Mantovani, A. (2012). Macrophage plasticity and polarization: in vivo veritas. J. Clin. Invest. *122*, 787–795.

24. Hori, S. (2014). Lineage stability and phenotypic plasticity of Foxp3$^+$ regulatory T cells. Immunol. Rev. *259*, 159–172.

25. Qian, C., and Cao, X. (2018). Dendritic cells in the regulation of immunity and inflammation. Semin. Immunol. *35*, 3–11.

26. Mulder, W.J.M., Ochando, J., Joosten, L.A.B., Fayad, Z.A., and Netea, M.G. (2019). Therapeutic targeting of trained immunity. Nat. Rev. Drug Discov. *18*, 553–566.

27. Sakaguchi, S., Miyara, M., Costantino, C.M., and Hafler, D.A. (2010). Foxp3$^+$ regulatory T cells in the human immune system. Nat. Rev. Immunol. *10*, 490–500.

28. Fang, R.H., Kroll, A.V., Gao, W., and Zhang, L. (2018). Cell membrane coating nanotechnology. Adv. Mater. *30*, e1706759.

29. Hu, C.M., Fang, R.H., Copp, J., Luk, B.T., and Zhang, L. (2013). A biomimetic nanosponge that absorbs pore-forming toxins. Nat. Nanotechnol. *8*, 336–340.

30. Hu, C.M., Fang, R.H., Luk, B.T., Chen, K.N., Carpenter, C., Gao, W., Zhang, K., and Zhang, L. (2013). Marker-of-self' functionalization of nanoscale particles through a top-down cellular membrane coating approach. Nanoscale *5*, 2664–2668.

31. Wei, X., Zhang, G., Ran, D., Krishnan, N., Fang, R.H., Gao, W., Spector, S.A., and Zhang, L. (2018). T-Cell-mimicking nanoparticles can neutralize HIV infectivity. Adv. Mater. *30*, e1802233.

32. Parodi, A., Quattrocchi, N., van de Ven, A.L., Chiappini, C., Evangelopoulos, M., Martinez, J.O., Brown, B.S., Khaled, S.Z., Yazdi, I.K., Enzo, M.V., et al. (2013). Synthetic nanoparticles functionalized with biomimetic leukocyte membranes possess cell-like functions. Nat. Nanotechnol. *8*, 61–68.

33. Molinaro, R., Corbo, C., Martinez, J.O., Taraballi, F., Evangelopoulos, M., Minardi, S., Yazdi, I.K., Zhao, P., De Rosa, E., Sherman, M.B., et al. (2016). Biomimetic proteolipid vesicles for targeting inflamed tissues. Nat. Mater. *15*, 1037–1046.

34. Kong, Y.Y., Feige, U., Sarosi, I., Bolon, B., Tafuri, A., Morony, S., Capparelli, C., Li, J., Elliott, R., McCabe, S., et al. (1999). Activated T cells regulate bone loss and joint destruction in adjuvant arthritis through osteoprotegerin ligand. Nature *402*, 304–309.

35. Komatsu, N., and Takayanagi, H. (2018). Immune-bone interplay in the structural damage in rheumatoid arthritis. Clin. Exp. Immunol. *194*, 1–8.

36. Bozec, A., Zaiss, M.M., Kagwiria, R., Voll, R., Rauh, M., Chen, Z., Mueller-Schmucker, S., Kroczek, R.A., Heinzerling, L., Moser, M., et al. (2014). T cell costimulation molecules CD80/86 inhibit osteoclast differentiation by inducing the IDO/tryptophan pathway. Sci. Transl. Med. *6*, 235ra60.

37. Manches, O., Fernandez, M.V., Plumas, J., Chaperot, L., and Bhardwaj, N. (2012). Activation of the noncanonical NF-κB pathway by HIV controls a dendritic cell immunoregulatory phenotype. Proc. Natl. Acad. Sci. U S A. *109*, 14122–14127.

38. Von Bubnoff, D., Scheler, M., Wilms, H., Fimmers, R., and Bieber, T. (2011). Identification of IDO-positive and IDO-negative human dendritic cells after activation by various proinflammatory stimuli. J. Immunol. *186*, 6701–6709.

39. Cederbom, L., Hall, H., and Ivars, F. (2000). CD4$^+$CD25$^+$ regulatory T cells down-regulate co-stimulatory molecules on antigen-presenting cells. Eur. J. Immunol. *30*, 1538–1543.

40. Xu, J., Liu, Y., Li, Y., Wang, H., Stewart, S., Van der Jeught, K., Agarwal, P., Zhang, Y., Liu, S., Zhao, G., et al. (2019). Precise targeting of POLR2A as a therapeutic strategy for human triple negative breast cancer. Nat. Nanotechnol. *14*, 388–397.

41. Qureshi, O.S., Zheng, Y., Nakamura, K., Attridge, K., Manzotti, C., Schmidt, E.M., Baker, J., Jeffery, L.E., Kaur, S., Briggs, Z., et al. (2011). Trans-endocytosis of CD80 and CD86: a molecular basis for the cell-extrinsic function of CTLA-4. Science *332*, 600–603.

42. Dhainaut, M., Coquerelle, C., Uzureau, S., Denoeud, J., Acolty, V., Oldenhove, G., Galuppo, A., Sparwasser, T., Thielemans, K., Pays, E., et al. (2015). Thymus-derived regulatory T cells restrain pro-inflammatory Th1 responses by downregulating CD70 on dendritic cells. EMBO J. *34*, 1336–1348.

43. Liang, B., Workman, C., Lee, J., Chew, C., Dale, B.M., Colonna, L., Flores, M., Li, N., Schweighoffer, E., Greenberg, S., et al. (2008). Regulatory T cells inhibit dendritic cells by lymphocyte activation gene-3 engagement of MHC class II. J. Immunol. *180*, 5916–5926.

44. Deaglio, S., Dwyer, K.M., Gao, W., Friedman, D., Usheva, A., Erat, A., Chen, J.F., Enjyoji, K., Linden, J., Oukka, M., et al. (2007). Adenosine generation catalyzed by CD39 and CD73 expressed on regulatory T cells mediates immune suppression. J. Exp. Med. *204*, 1257–1265.

45. Vignali, D.A., Collison, L.W., and Workman, C.J. (2008). How regulatory T cells work. Nat. Rev. Immunol. *8*, 523–532.

46. Redlich, K., and Smolen, J.S. (2012). Inflammatory bone loss: pathogenesis and therapeutic intervention. Nat. Rev. Drug Discov. *11*, 234–250.

47. Marchesan, J., Girnary, M.S., Jing, L., Miao, M.Z., Zhang, S., Sun, L., Morelli, T., Schoenfisch, M.H., Inohara, N., Offenbacher, S., et al. (2018). An experimental murine model to study periodontitis. Nat. Protoc. *13*, 2247–2267.

48. Papapanou, P.N., Sanz, M., Buduneli, N., Dietrich, T., Feres, M., Fine, D.H., Flemmig, T.F., Garcia, R., Giannobile, W.V., Graziani, F., et al. (2018). Periodontitis: consensus report of workgroup 2 of the 2017 world workshop on the classification of periodontal and peri-implant diseases and conditions. J. Periodontol. *89* (*Suppl 1*), S173–S182.

49. Ephrem, A., Epstein, A.L., Stephens, G.L., Thornton, A.M., Glass, D., and Shevach, E.M. (2013). Modulation of Treg cells/T effector function by GITR signaling is context-dependent. Eur. J. Immunol. *43*, 2421–2429.

50. Samanta, A., Li, B., Song, X., Bembas, K., Zhang, G., Katsumata, M., Saouaf, S.J., Wang, Q., Hancock, W.W., Shen, Y., et al. (2008). TGF-beta and IL-6 signals modulate chromatin binding and promoter occupancy by acetylated Foxp3. Proc. Natl. Acad. Sci. U S A *105*, 14023–14027.

51. Nie, H., Zheng, Y., Li, R., Guo, T.B., He, D., Fang, L., Liu, X., Xiao, L., Chen, X., Wan, B., et al. (2013). Phosphorylation of Foxp3 controls regulatory T cell function and is inhibited by TNF-α in rheumatoid arthritis. Nat. Med. *19*, 322–328.

52. Glowacki, A.J., Yoshizawa, S., Jhunjhunwala, S., Vieira, A.E., Garlet, G.P., Sfeir, C., and Little, S.R. (2013). Prevention of inflammation-mediated bone loss in murine and canine periodontal disease via recruitment of regulatory lymphocytes. Proc. Natl. Acad. Sci. U S A *110*, 18525–18530.

53. Lan, P., Zhou, B., Tan, M., Li, S., Cao, M., Wu, J., and Lei, M. (2020). Structural insight into precursor ribosomal RNA processing by ribonuclease MRP. Science *369*, 656–663.

54. Chaturvedi, A., Dorward, D., and Pierce, S.K. (2008). The B cell receptor governs the subcellular location of Toll-like receptor 9 leading to hyperresponses to DNA-containing antigens. Immunity *28*, 799–809.